Airborne Wind Energy – to fly or not to fly?

A STUDY ON THE POWER PRODUCTION OF AIRBORNE WIND ENERGY SYSTEMS AND THEIR INTEGRATION IN THE ELECTRICITY GENERATION SYSTEM

ELENA C. MALZ

Department of Electrical Engineering
CHALMERS UNIVERSITY OF TECHNOLOGY

Göteborg, Sweden 2020

To my friends and family
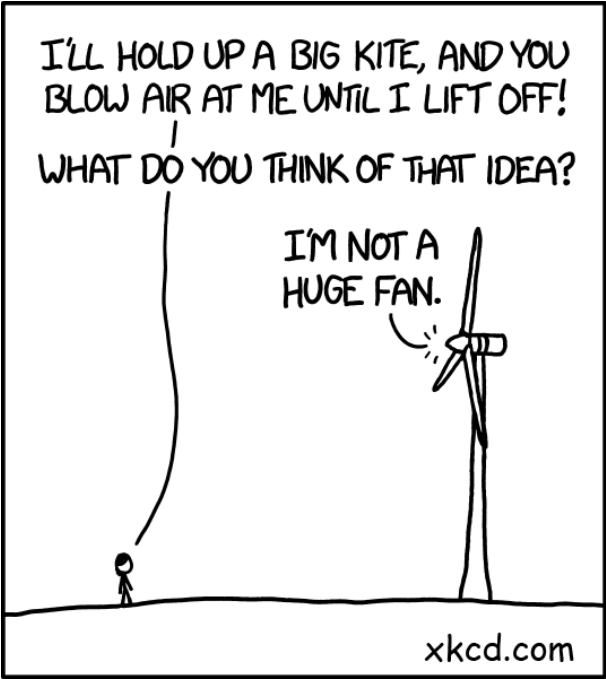
Abstract

This thesis investigates crosswind Airborne Wind Energy Systems (AWESs) in terms of power production and potential role in future electricity generation systems. The perspective ranges from the small scale, modelling AWE as a single system, to the large, implementing AWESs in regional electricity systems.

To estimate the AWES power production, the thesis provides a dynamic system model that serves as the basis for all the work. The model describes the flight dynamics of a rigid wing that is exposed to tether and aerodynamic forces controlled by flight control surfaces. Index-3 Differential Algebraic Equations (DAEs) based on Lagrangian mechanics describe the dynamics. This model is validated by fitting it to real flight measurements obtained with a pumping-mode AWES, the prototype AP2 by Ampyx Power. The optimal power production of an AWES depends on complex trade-offs; this motivates formulating the power production computation as an Optimal Control Problem (OCP). The thesis presents the numerical methods needed to discretize the OCP and solve the resulting Nonlinear Program (NLP).

Large-scale implementation of AWESs raises challenges related to variability in power production on the time scale of minutes to weeks. For the former, we investigate the periodic fluctuations in the power output of a single AWES. These fluctuations can be severe when operating a wind farm and have to be considered and reduced for an acceptable grid integration. We analyse the option of controlling the flight trajectories of the individual systems in a farm so that the total power output of the farm is smoothed. This controlled operation fixes the system's trajectory, reducing the ability to maximize the power output of individual AWESs to local wind conditions. We quantify the lost power production if the systems are controlled such that the total farm power output is smoothed. Results show that the power difference between the optimal and fixed trajectory does not exceed 4% for the systems modelled in the study.

The variations in AWESs power production on the timescale of hours to weeks are particularly relevant to the interaction between AWE and other power generation technologies. Investigating AWESs in an electricity system context requires power-generation profiles with high spatio-temporal resolution, which means solving a large number of OCPs. In order to efficiently solve these numerous OCPs in a sequential manner, this thesis presents a homotopy-path-following method combined with modifications to the NLP

solver. The implementation shows a 20-fold reduction in computation time compared to the original method for solving the NLP for AWES power optimization. For large wind-data sets, a random forest regression model is trained to a high accuracy, providing an even faster computation. The annual generation profiles for the modelled systems are computed using ERA5 wind data for several locations and compared to the generation profile for a traditional wind turbine. The results show that the profiles are strongly correlated in time, which is a sobering fact in terms of technology competition. However, the correlation is weaker in locations with high wind shear.

The potential role of AWESs in the future electricity system is further investigated. This thesis implements annual AWE-farm generation profiles into a cost-optimizing electricity system model. We find that AWE is most valuable to the electricity system if installed at sites with low wind speed within a region. At greater shares of the electricity system, even if AWESs could demonstrate lower costs compared to wind turbines, AWE would merely substitute for them instead of increasing the total share of wind energy in the system. This implies that the economic value of an AWES is limited by its cost relative to traditional wind turbines.

Keywords: Airborne wind energy, Renewable energy systems, Modelling, Optimal control

Acknowledgements

iv

List of Publications

This thesis is based on the following appended papers:

Paper A
E.C Malz, J. Koenemann, S. Sieberling, and S. Gros, "A reference model for airborne wind energy systems for optimization and control", *Renewable Energy*, Vol. 140, 2019.

Paper B
E.C. Malz, V. Verendel, S. Gros, "Computing the power profiles for an airborne wind energy system based on large-scale wind data", in press in *Renewable Energy*, 2020.

Paper C
E.C. Malz, M. Zanon, S. Gros, "A quantification of the performance loss of power averaging in airborne wind energy farms", *European Control Conference (ECC)*, 2018.

Paper D
E.C. Malz, F. Hedenus, L.Göransson, V.Verendel, S. Gros, "Drag-mode airborne wind energy vs. wind turbines: An analysis of power production, variability and geography", *Energy*, Vol. 139, 2020.

Paper E
E.C. Malz, V. Walter, L. Göransson, S. Gros, "The value of AWE systems in the future electricity system", submitted to *Wind Energy, Wiley*, 2020.

Other related publications by the author not included in this thesis:

[i] R. Leuthold, J. De Schutter, **E.C. Malz**, G. Licitra, S. Gros, M. Diehl, "Operational regions of a multi-kite AWE system", *European Control Conference (ECC)*, 2018.

Acronyms

AWE	Airborne Wind Energy
AWES	Airborne Wind Energy System
DAE	Differential Algebraic Equation
DCM	Direct Cosine Matrix
FLH	Full Load Hour
IP	Interior Point
LDC	Load Duration Curve
LICQ	Linear Independence Constraint Qualification
LP	Linear Programming
MILP	Mixed-Integer Linear Programming
MSV	Marginal System Value
NLP	Nonlinear Program
OCP	Optimal Control Problem
ODE	Ordinary Differential Equation
PDIP	Primal-Dual Interior Point
SOSC	Second Order Sufficient Condition
WT	Wind Turbine

Contents

Part I

Introductory Chapters

1

Introduction

In 1752 Benjamin Franklin proposed an experiment to collect electric energy from the air during thunderstorms using a kite and a conductive wire. Whether Franklin ever actually conducted that specific experiment is controversial, but, either way, the method has not proven to be a useful way of capturing electricity. In 1980 the engineer Miles L. Loyd published a new idea for using a kite to harvest energy: flying a tethered kite crosswind to produce enough lift to support the kite and generate power. Kites had been used to pull loads on the ground before that but not to generate power. Loyd introduced two different modes for crosswind kites, lift mode and drag mode, with similar power potentials. Lift mode, also known as pumping mode, applies the tether force to a rotating drum. Drag mode adds additional drag to the kite in form of power-generating propellers. Loyd's paper is generally considered to mark the beginning of Airborne Wind Energy (AWE) as an object of study. Loyd claimed that kites are able to harvest a higher energy density than traditional wind power technologies, as a larger area can be swept through and higher altitudes can be reached. However, the future role of AWE systems is still uncertain. Broader knowledge about AWE power production and its interaction with the rest of the power system is therefore required in order to support decision-making regarding technology design and system siting.

1.1   Airborne wind energy

As of today, there is no commercial Airborne Wind Energy System (AWES), but some businesses are building and testing prototypes with a capacity of up to several $100\,\text{kW}$ [1–6]. Several different system concepts exist, "ground-gen" and "fly-gen" types, as well as crosswind and non-crosswind types [7–

9]. Non-crosswind types include drone-based systems and aerostatic (lighter-than-air) systems with turbines in helium-filled balloons. This thesis focuses on crosswind types. Most of the companies are pursuing the ground-gen technology [1–4]. The ground-gen technology is based on rigid, semi-rigid, or soft wings and ground-based generators connected to drums. The kite is tethered to the drum so that crosswind flight pulls out a cable, generating rotational energy at the drum. The rotational energy is then transformed to electrical energy with a generator. While pulling out the tether, the wing flies in a circular or figure-of-eight trajectory. At the maximum tether length, the wing is retracted using a fraction of the energy that has been generated. The overall energy generated by one "flight period" remains positive. Optimally, the tether is reeled out at a speed that is one third the prevailing wind speed [10], while the reel-in takes place at minimal energy expense. Here, we refer to this as the pumping mode. The other crosswind concept, known as the drag mode, instead has electric generators on board in the form of small propellers [11]. The concept is based on rigid wings that are able to carry the generators and manage high-velocity flights. The lift generated during flight is transformed into a forward motion that is used by the propellers to generate electricity. The electricity is transferred via the tether to the ground station. Fig. 1.1 displays the two crosswind AWESs.
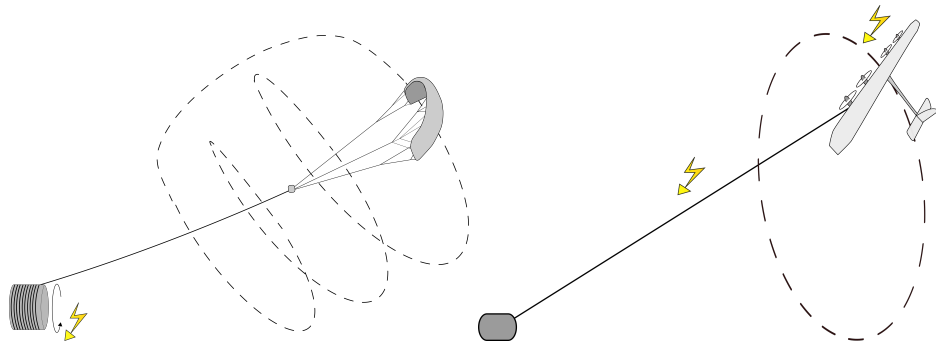
Figure 1.1: Illustration of pumping-mode system with a soft wing (left) and drag-mode system (right). Pumping-mode systems may have rigid, semi-rigid, or soft wings.

1.1.1 Benefits and challenges of AWE

The appeal of AWESs lies in the potential for reducing the amount of materials used and increasing the altitudes reached, compared to traditional wind systems. Turbine towers are growing taller and rotor diameters are also increasing to harvest stronger and steadier winds, with hub heights reaching around 165 m, leading to an upper blade-tip height above 200 m [12].

However, the taller the turbine tower, the higher the total wind turbine costs, leading to current cost-optimal tower heights of around 110 m [13]. Along with the boom in wind power technology comes the criticism of the amounts of materials used and the lack of recycling solutions. The weight of a single blade can reach 35 metric tons [14]. On top of that, in many regions "nimbyism"[1] impedes the implementation of new turbines due to audiovisual noise.

For AWESs, the visual impact and resource use are claimed to be less of an issue. The greater operational altitude reduces the visual impact, and when there is little wind, systems are landed and disappear completely from the field of vision. Early theoretical studies promise a reduction in materials and lower costs compared to conventional wind turbines [7]. Current cost estimates range between $33 \, \text{€}/\text{MWh}$ and $150 \, \text{€}/\text{MWh}$ [3, 4, 15, 16]. AWESs can access high-altitude winds and are not constrained by the construction height and the cost of a heavy, material-intensive tower. The operational altitude is planned to be between 300-600 m, aiming for stronger and steadier winds [1, 4, 11]. The possibility of adjusting the height offers the additional advantage of being able to chase the best winds and limit wake effects [17]. As a result, AWESs are aiming for a higher wind-power yield than conventional turbines. Given these aspects, the community expects that AWESs will have advantages over traditional wind turbines.

Several companies are delivering promising results from well-functioning small-scale prototypes, with some even close to commercialization [1, 4]. According to a report by the European Commission [15], small devices in the range of 100 kW may serve as a potential entry to the market as they can exploit niche areas where electricity prices are high. However, in order to have a high impact and eventually contribute to the European decarbonization target, large-scale systems should be pursued.

For large-scale deployment, the challenges and barriers to overcome have been documented and summarized in the European Commission report [15]. The main concerns relate to system safety and reliability, which influence social acceptance and regulatory approval. These aspects are crucial as they define the horizontal space available for exploitation. Also, strict compliance with airspace regulations is important, as these define the vertical exploitable space. The report also mentions the necessity of further investigations of wind resources, the power potential of AWESs, and the competition with well-established renewable energy technologies. Regarding the last point, successful commercialization of AWE would benefit from AWE

---

[1]NIMBY: Not In My Back Yard; nimbyism: an attitude towards a phenomenon, which is typically positive/neutral so long as the phenomenon does not directly affect the subject, at which point it turns negative.

reaching sites and resources that would otherwise remain unexploited. It would also be advantageous if the temporal generation profiles for AWESs differ from existing generation profiles or if the electricity generation costs are significantly lower compared to existing technologies [15].

1.2 Research motivation

As of today, only a few studies have been published on the actual power generation potential of AWESs, the related technology-competition and complementarity issues expressed in the European Commission report [15]. Such investigations are crucial for guiding incentives and avoiding misplaced investments.

Investigating the potential for AWE requires analysing the wind resource (cf. [18–20]). In addition, it is also important to take the transformation from wind energy to electrical energy into account. The actual power production of an AWES can be estimated with the help of a mathematical model sophisticated enough to both capture system boundaries that may limit power generation and optimize operation to maximize power generation. This requires a model that simulates wing flight dynamics and optimizes flight trajectories for power generation given prevailing wind conditions. With the help of such a model, the maximal power generation and the optimal flight trajectory can be estimated for any given external parameters, representing wind conditions, wing characteristics, and tether dimensions, etc. Further, it can be used to assess the potential power generation for any wing size and any location where wind data are available. Here, annual generation profiles can be obtained and then compared to generation profiles for other technologies in order to investigate technology competition and assess the economic value of AWE.

1.3 Thesis contribution

The main contributions of the thesis are as follows:

- A model of an AWES is presented and validated with flight measurements from a prototype wing. The model is built as a dynamic system based on differential algebraic equations. The wing is approximated as a point mass with six degrees of freedom. The main purpose of the model is to estimate the power generation and accurately simulate the system's flight trajectory, taking into account weather- and

design-dependent parameters. The thesis describes the model formulation in such detail that it can serve as a reference model for the community.

- The model is implemented in an Optimal Control Problem (OCP) in order to maximize the average power generation by optimizing the flight orbit with respect to external conditions. In order to perform large-scale analyses, a methodology is presented that computes annual generation profiles based on realistic highly resolved wind data. The methodology proposes an algorithm that reduces the computational effort in solving the large numbers of OCPs that need to be handled individually for each evaluated wind condition.

- The generated power of an AWES varies greatly within one cycle, which lasts less than a minute. This thesis investigates an approach that involves synchronizing and phase-shifting the cycles of several systems in a farm to yield a fairly constant farm power output. The difference relative to the results obtained by optimizing the individual system trajectories for maximal power is quantified.

- The interplay of AWESs and traditional wind turbines (WTs) is investigated by analysing and comparing annual electricity generation profiles at several locations. The comparison is quantified in terms of the Gini coefficient, the generation duration curve, and the Pearson correlation coefficient in order to evaluate the distribution of the generation over time. Further, the annual electricity generation and the number of hours with high and low generation are estimated as well as the differences in the generation profiles between AWESs and WTs.

- The value of AWE to the electricity generation system is estimated for four different regional systems with varying resource conditions for wind and solar power generation. The estimate is made by integrating the generation profiles of AWESs into a cost-minimizing electricity-system investment model. The results deliver an understanding of the interactions between AWESs, WTs, and other power generating technologies. An AWE investment cost is estimated, corresponding to the cost allowed to achieve cost-competitiveness in the modelled future electricity system.

1.4 Outline

The thesis is structured as follows. Chapter 2 introduces and defines key concepts and methods. Chapter 3 presents the mathematical models used

to perform the studies. The model formulations are presented in detail and the data sets used are listed. Chapter 4 applies the developed methods to investigate the power generation of the modelled AWESs. The value of the AWESs is investigated by comparing the results to the power generated by traditional wind turbines and by integrating the AWE technology in a model of the electricity system. Results are presented and discussed. Chapter 5 summarizes the content of the publications. Chapter 6 discusses and concludes the thesis work and highlights the main findings.

2
Preliminaries

This chapter provides an introduction to the concepts and methods used in this thesis. The descriptions and explanations draw upon [21–23], among other work.

2.1 Dynamic systems

Dynamic systems are widely used to describe processes that evolve over time and space. Depending on the process, the dynamic system can be deterministic or stochastic. Another distinction is made between continuous, discrete, and hybrid systems. This thesis uses deterministic continuous and discrete systems, formulated as Ordinary Differential Equations (ODEs) or Differential Algebraic Equations (DAEs).

Lagrangian mechanics
Physical systems can be described with classical Newtonian mechanics or, alternatively, with Lagrangian mechanics. Both are based on the same laws of mechanics, but use different approaches to describe the motions of the system. Unlike Newtonian mechanics, Lagrangian mechanics is not formulated directly with the classical laws of mechanics, but with the kinetic and potential energies of the masses available in the system. Newtonian mechanics is the standard approach for describing a single system and may include non-conservative forces, e.g. friction. Lagrangian mechanics is ideal for describing conservative forces and multi-body systems that move in different reference frames. The model used here is formulated using Lagrangian dynamics in order to reduce complexity.

Definition 2.1. (Continuous-time controlled dynamic system) Let us define time $t \in \mathbb{R}$, differential states $x \in \mathbb{R}^{n_x}$, algebraic variables $z \in \mathbb{R}^{n_z}$, control

inputs $u \in \mathbb{R}^{n_u}$, and parameters $p \in \mathbb{R}^{n_p}$. A continuous-time controlled dynamic system can then be defined as an implicit function

$$F(x(t), \dot{x}(t), u(t), z(t), p) = 0, \tag{2.1}$$

where $\dot{x}(t) \in \mathbb{R}^{n_x}$ defines the time-differentiated states $\frac{dx(t)}{dt}$. The algebraic states $z(t)$ do not appear in time-differentiated form in the dynamics. The inputs $u(t)$ are the control inputs to the system. The parameters p are constant parameters that are not always explicitly specified.

Function (2.1) describes a *fully implicit* Differential Algebraic Equation (DAE). The differential and algebraic equations can also be split, resulting in a *semi-explicit DAE*

$$\dot{x} = f(x(t), z(t), u(t), p) \tag{2.2a}$$

$$0 = g(x(t), z(t), u(t), p). \tag{2.2b}$$

If a system does not contain any algebraic states, the model becomes an Ordinary Differential Equation (ODE). Unlike ODEs, DAEs have a differential index, which denotes the number of times the system equations have to be time-differentiated in order to become an ODE. DAEs with an index higher than one are defined as "high-index DAEs" and are numerically harder to treat than index-1 DAEs or ODEs. The easiest way to treat high-index DAEs is via index-reduction such that they can be solved with classical integration methods (presented below). When performing an index-reduction, it is important to collect the algebraic equations on which a time differentiation is performed and add them as "consistency conditions". Consistency conditions need to be taken into account when simulating the system.

2.1.1   Numerical integration methods

Simulating a system such as (2.1) entails solving the index-1 DAE or the ODE starting at an initial value $x(0)$. These problems are also known as *Initial Value Problems* (IVPs). Unless the equations are simple, the system can rarely be solved exactly because an analytical solution cannot be obtained. Instead, the state trajectories $x(t), z(t)$ are approximated over a certain time interval $[0, T]$ by means of numerical methods, often referred to as integrators. One can distinguish between one-step and multi-step integrators as well as explicit and implicit integrators. For simplicity, in the following we first assume an IVP in the form of an explicit ODE

$$\dot{x}(t) = f(x(t), u(t)), \quad x(0) = x_0, \quad t \in [0, T]. \tag{2.3}$$

To generate the solution approximation of the IVP, the time interval [0,T] is discretized by dividing it into M subintervals to a time grid as $[0, t_k, t_{k+1}, \ldots, T]$. For simplicity, we set the step size h to be constant: $h = t_{k+1} - t_k = \frac{T}{M}$.

Explicit Euler integrator

The simplest integrator is the one-step explicit *Euler step integration*

$$\tilde{x}_{k+1} = \tilde{x}_k + hf(\tilde{x}_k, u_k), \quad \text{for } k = 0, \ldots, M - k, \tag{2.4}$$

in which the state trajectory is linearly approximated between t_k and t_{k+1}. The gradient of the linear extrapolation equals the time derivative $\dot{x}_k = f(x_k, u_k)$ at the current time step k, assuming a constant control input u_k over the discretized time interval h. At $k = 0$, the state is given as x_0, while the states at $k > 0$ are the approximated states of the integration denoted $\tilde{x}_k$. The Euler step method becomes a good approximation if the time steps h are small. However, there exist more computationally efficient integrators such as *Runga-Kutta* (RK) methods. The most commonly used is the fourth-order RK4.

Implicit integrators

In order to solve implicit systems such as (2.1), implicit integrators are preferable. Implicit integrators show a more complex structure, but, unlike explicit integrators, they are stable independent of the step size h. Here, we use a special case of the implicit RK method, the so-called *orthogonal collocation* method, to solve the implicit model functions. Orthogonal collocation methods approximate the state trajectories with orthogonal polynomials, e.g. Lagrange polynomials, see below.

Lagrange polynomials

The polynomial is generated by a linear combination of weighted Lagrange polynomials

$$p_{\mathcal{L}}(\psi, \theta) = \sum_{i=1}^{J} \theta_i \cdot \ell_i(\psi) = \sum_{i=1}^{J} \theta_i \cdot \prod_{\substack{j=1 \\ j \neq i}} \frac{\psi - \psi_j}{\psi_i - \psi_j}, \tag{2.5}$$

where $\psi_i \in [0, 1]$ and J is the number of polynomials. The Lagrange polynomials ℓ show the special feature of being orthogonal $\int_0^1 \ell_i(\psi)\ell_j(\psi)d\psi = 0$, if $j \neq i$ and satisfying

$$\ell_i(\psi_j) = \begin{cases} 1, & \text{if } i = j \\ 0, & \text{otherwise.} \end{cases} \tag{2.6}$$

This means that

$$P_{\mathcal{L}}(\psi_i, \theta) = \theta_i, \quad i = 1, \ldots, J, \qquad (2.7)$$

which is an important property for using the polynomials for the collocation integration method. The Lagrange polynomials with ℓ_i for the case of four $J = 5$ data points are illustrated in Fig. 2.1 on the left. Here, the values of ψ correspond to the Radau collocation points [23]. Adding the individual polynomials and weighting them with $\theta = [1, 2, 5, 2, 3]$ generates a polynomial $p_{\mathcal{L}}(\psi, \theta)$ (visible on the right), and we can see that (2.7) holds.
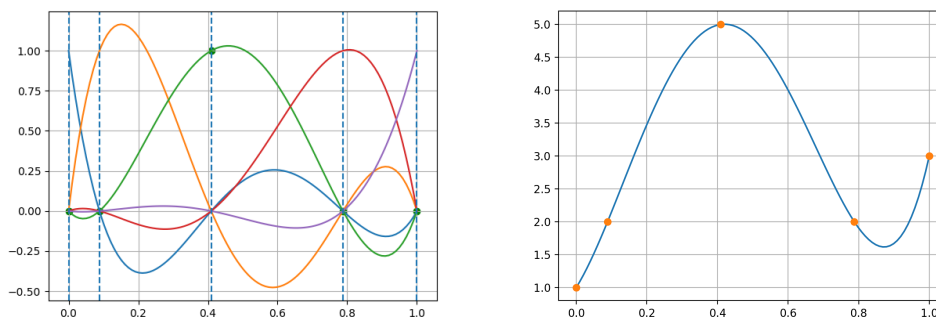
Figure 2.1: Visualization of a Lagrange polynomial. Left: The individual Lagrange polynomials ℓ_i. Right: The resulting polynomial with the sample coefficients $\theta = [1, 2, 5, 2, 3]$ at $\psi = [0.0, 0.09, 0.41, 0.78, 1.0]$ (Radau collocation points of degree 4).

Orthogonal collocation

Using the orthogonal collocation method, the state trajectory is approximated between a time interval $[t_k, t_{k+1}]$ with Lagrange polynomials as Eq. (2.5). The coefficients θ are individual for each interval and need to be chosen such that the system dynamics f are enforced on the collocation points ψ_i of the polynomial and its derivative, such that

$$\begin{aligned} p_{\mathcal{L}}(t_{k,i}, \theta_{k,i}) &= x_{k,i} \\ \frac{\partial\, p_{\mathcal{L}}(t_{k,i}, \theta_{k,i})}{\partial\, t} &= f(x_{k,i}, u_k), \end{aligned} \qquad (2.8)$$

where $t_{k,i}$ equals $t_k + \psi_i$ and $x_{k,i}$ is the state at $t_{k,i}$. Due to the characteristics of a Lagrange polynomial, it holds that

$$f(x_{k,i}, u_k) = f(p_{\mathcal{L}}(t_{k,i}, \theta_{k,i}), u_k) = f(\theta_{k,i}, u_k). \qquad (2.9)$$

The Lagrange polynomial $p_{\mathcal{L}}$ can alternatively be set equal to the dynamic function f, such that the state trajectory is the integral of the polynomial $p_{\mathcal{L}}$. In Section 2.3.1, the topic of collocation integration is continued as it is used in the direct optimal control method.

2.2 Optimization problems

In this thesis we are mainly concerned with two types of optimization problems: a dynamic nonlinear problem within an optimal control framework and a static linear programming problem. This section presents the basics of both problem types. Vectors are denoted with bold letters.

2.2.1 Static constrained optimization

The general form of a static constrained optimization is

$$
\begin{aligned}
\min_{\mathbf{w} \in \mathbb{R}} \quad & \Phi(\mathbf{w}) \\
\text{s.t.} \quad & \mathbf{g}(\mathbf{w}) = 0, \\
& \mathbf{h}(\mathbf{w}) \leq 0,
\end{aligned}
\tag{2.10}
$$

where $\mathbf{w} \in \mathbb{R}^{n_\mathrm{w}}$ is a vector of n_w (continuous) decision variables, often comprising the states $\mathbf{x}$, algebraic variables $\mathbf{z}$, and control inputs $\mathbf{u}$. $\Phi(\mathbf{w})$ is the objective function that is to be minimized, $\mathbf{g}(\mathbf{w})$ are the equality constraints, and $\mathbf{h}(\mathbf{w})$ are the inequality constraints. The functions $\Phi : \mathbb{R}^{n_\mathrm{w}} \to \mathbb{R}$, $\mathbf{g} : \mathbb{R}^{n_\mathrm{w}} \to \mathbb{R}^{n_\mathrm{g}}$, and $\mathbf{h} : \mathbb{R}^{n_\mathrm{w}} \to \mathbb{R}^{n_\mathrm{h}}$ are assumed to be smooth and at least twice continuously differentiable. The general form of (2.10) normally describes a Nonlinear Program (NLP).

Definition 2.2. (Feasibility) If $\mathbf{w}^\star \in \mathcal{F} := \{\mathbf{w} | \mathbf{g}(\mathbf{w}) = 0, \mathbf{h}(\mathbf{w}) \leq 0\}$, the point $\mathbf{w}^\star$ is feasible.

Definition 2.3. (Global minimum) The point $\mathbf{w}^\star$ is a global minimum if

$$
\forall \mathbf{w} \in \mathcal{F} : \Phi(\mathbf{w}^\star) \leq \Phi(\mathbf{w}).
$$

Definition 2.4. (Local minimum) The point $\mathbf{w}^\star$ is a local minimum if there exists a neighbourhood $\mathcal{N}$ around $\mathbf{w}^\star$ such that

$$
\forall \mathbf{w} \in \mathcal{F} \cap \mathcal{N} : \Phi(\mathbf{w}^\star) \leq \Phi(\mathbf{w}).
$$

Definition 2.5. (Active constraints and active sets) An inequality constraint $\mathbf{h}_i$ is *active* if $\mathbf{h}_i(\mathbf{w}) = 0$ and otherwise *inactive*. We can further define an active set for all feasible points $\mathbf{w} \in \mathcal{F}$ that fulfil $\mathbf{h}(\mathbf{w}) = 0$. The active set is defined as

$$
\mathcal{A}(\mathbf{w}) := \{i | \mathbf{h}_i(\mathbf{w}) = 0\}.
$$

Sometimes, the active set is defined to comprise all active constraints, i.e. to include the equality constraints.

In the special case of the functions $\Phi, \mathbf{g}, \mathbf{h}$ being linear, (2.10) becomes a Linear Programming (LP) problem, which is then commonly formulated as

$$
\begin{aligned}
\min_{w \in \mathbb{R}} \quad & \Phi = \mathbf{c}^\top \mathbf{w} \\
\text{s.t.} \quad & \mathbf{A}\mathbf{w} - \mathbf{b} = 0, \\
& \mathbf{C}\mathbf{w} - \mathbf{d} \geq 0, \\
& \mathbf{w} \geq 0,
\end{aligned}
\tag{2.11}
$$

where $\mathbf{w} \in \mathbb{R}^{n_{\mathrm{w}}}$, $\mathbf{c} \in \mathbb{R}^{n_{\mathrm{w}}}$, $\mathbf{A} \in \mathbb{R}^{n_{\mathrm{g}} \times n_{\mathrm{w}}}$, $\mathbf{b} \in \mathbb{R}^{n_{\mathrm{g}}}$, $\mathbf{C} \in \mathbb{R}^{n_{\mathrm{h}} \times n_{\mathrm{w}}}$, and $\mathbf{d} \in \mathbb{R}^{n_{\mathrm{h}}}$. If $\mathbf{w}$ also contains integer variables, the problem becomes a Mixed-Integer Linear Programming (MILP) problem. Here, however, $\mathbf{w}$ consists of continuous variables, only.

2.2.2 Optimality conditions for constrained nonlinear problems

In a constrained NLP, the first- and second-order optimality conditions are important for identifying the optimality of a candidate point $\mathbf{w}$. In order to define the optimality conditions, some other concepts need to be covered first.

A point $\mathbf{w}$ is *regular* if it satisfies the regularity conditions (also called "constraint qualifications"). Among the many different regularity conditions, one of the most common is the Linear Independence Constraint Qualification (LICQ).

Definition 2.6. (LICQ) The Linear Independence Constraint Qualification (LICQ) holds if the gradients of the active constraints

$$
\nabla \mathbf{g}(\mathbf{w}^\star), \ \nabla \mathbf{h}_i(\mathbf{w}^\star), \ \forall i \in \mathcal{A}(\mathbf{w}^\star)
$$

are linearly independent at the optimal solution $\mathbf{w}^\star$.

If the active constraints are stacked as

$$
\tilde{\mathbf{g}} = \left[\begin{array}{l} \mathbf{g}(\mathbf{w}^\star) \\ \mathbf{h}_i(\mathbf{w}^\star) \quad \text{for} \quad i \in \mathcal{A}(\mathbf{w}^\star) \end{array} \right],
\tag{2.12}
$$

LICQ is also equivalent to the full row rank of the Jacobian matrix $\frac{\partial \tilde{\mathbf{g}}}{\partial \mathbf{w}}(\mathbf{w}^\star)$.

Definition 2.7. (Lagrangian function) The Lagrangian function of an optimization problem is defined as $\mathcal{L}(\mathbf{w}, \boldsymbol{\nu}, \boldsymbol{\mu}) = \Phi(\mathbf{w}) + \mathbf{g}(\mathbf{w})^\top \boldsymbol{\nu} + \mathbf{h}(\mathbf{w})^\top \boldsymbol{\mu}$, where $\Phi(\mathbf{w})$ is the cost function, and $\boldsymbol{\nu}$ and $\boldsymbol{\mu}$ the Lagrange multipliers for the equality $\mathbf{g}(\mathbf{w})$ and inequality $\mathbf{h}(\mathbf{w})$ constraints, respectively.

Definition 2.8. (Karush-Kuhn-Tucker / First-order necessary conditions)
Let an optimal point $\mathbf{w}^\star$ satisfy LICQ, then there exist unique Lagrange
multipliers $\boldsymbol{\nu}^\star$, $\boldsymbol{\mu}^\star$ that fulfil the Karush-Kuhn-Tucker (KKT) conditions,
which are defined as

$$
\begin{aligned}
\nabla_\mathbf{w}\mathcal{L}(\mathbf{w}^\star,\boldsymbol{\nu}^\star,\boldsymbol{\mu}^\star) =\ & \nabla_\mathbf{w}\Phi(\mathbf{w}^\star) + \nabla_\mathbf{w}\mathbf{g}(\mathbf{w}^\star)\boldsymbol{\nu}^\star + \nabla_\mathbf{w}\mathbf{h}(\mathbf{w}^\star)\boldsymbol{\mu}^\star && \text{(2.13a)} \\
\mathbf{g}(\mathbf{w}^\star) =\ & 0 && \text{(2.13b)} \\
\mathbf{h}(\mathbf{w}^\star) \leq\ & 0 && \text{(2.13c)} \\
\boldsymbol{\mu}^\star \geq\ & 0 && \text{(2.13d)} \\
\boldsymbol{\mu}^{\star\top}\mathbf{h}(\mathbf{w}^\star) =\ & 0, && \text{(2.13e)}
\end{aligned}
$$

where (2.13a) represents the dual conditions and can be seen as a force
equilibrium at the stationary point, (2.13b) and (2.13c) are the constraints
and primal conditions, and (2.13e) represents the complementary slackness
conditions, given that (2.13d) holds. The proof can be found in [23].

The complementary slackness conditions (2.13e) define for each constraint a
non-smooth manifold which is non-differentiable at the origin. A constraint
is called *active* if $\mathbf{h}_i(\mathbf{w}^\star) = 0$, $\boldsymbol{\mu}_i^\star < 0$ and *inactive* if $\mathbf{h}_i(\mathbf{w}^\star) < 0$, $\boldsymbol{\mu}_i^\star = 0$. A
constraint is called *weakly active* if $\mathbf{h}_i(\mathbf{w}^\star) = 0$, $\boldsymbol{\mu}_i^\star = 0$.
If the NLP is convex, the first-order necessary conditions are also sufficient
conditions.

Definition 2.9. (Strict complementarity) Strict complementarity holds for
a KKT point $(\mathbf{w}^\star,\boldsymbol{\nu}^\star,\boldsymbol{\mu}^\star)$ if all active constraints are strictly active, i.e.

$$
\boldsymbol{\mu}_i^\star < 0 \qquad \forall i \in \mathcal{A}(\mathbf{w}^\star).
$$

Definition 2.10. (KKT point) A point $(\mathbf{w}^\star,\boldsymbol{\nu}^\star,\boldsymbol{\mu}^\star)$ is called a KKT point
or a primal-dual solution if it satisfies conditions (2.13). Let an optimal
point $\mathbf{w}^\star$ satisfy LICQ, then there exist unique Lagrange multipliers $\boldsymbol{\mu}^\star$, $\boldsymbol{\nu}^\star$
that fulfil the KKT conditions.

Definition 2.11. (SOSC) In most cases, the necessary condition (LICQ)
is not sufficient for defining optimality. Then, the Second Order Sufficient
Condition (SOSC) has to hold such that a point $(\mathbf{w}^\star,\boldsymbol{\mu}^\star,\boldsymbol{\nu}^\star)$ can be defined
as a KKT point. SOSC holds if the Hessian of the Lagrangian is strictly
positive on the null space of the strictly active constraints, i.e.

$$
\mathbf{d}^\top\nabla_\mathbf{w}^2\mathcal{L}(\mathbf{w}^\star,\boldsymbol{\nu}^\star,\boldsymbol{\mu}^\star)\mathbf{d} > 0, \qquad \forall \mathbf{d} \in \mathcal{N}_{\tilde{g}} \setminus 0,
$$

where $\mathcal{N}_{\tilde{g}}$ is the null space of the strictly active constraints

$$
\mathcal{N}_{\tilde{g}} := \{\mathbf{d} \,|\, \nabla_\mathbf{w}\tilde{\mathbf{g}}^\top\mathbf{d} = 0\}
$$

and $\mathbf{d}$ the base vector of the matrix, or the "free directions" that are not fixed by constraints.

The projection of the Hessian on the null space of the Jacobian in (2.11) is called the *reduced Hessian* and can be conceived of as the local curvature around the optimum $\mathbf{w}^\star$ in the "free" directions. Strict SOSC is then related to a strictly positive curvature along the directions $\mathbf{d}$.

2.2.3   Parametric NLPs

Parametric NLPs include parameters $\mathbf{p}$ as

$$
\begin{aligned}
\min_{\mathbf{w}} \quad & \Phi(\mathbf{w}, \mathbf{p}) \\
\text{s.t.} \quad & \mathbf{g}(\mathbf{w}, \mathbf{p}) = 0, \\
& \mathbf{h}(\mathbf{w}, \mathbf{p}) \leq 0.
\end{aligned}
\tag{2.14}
$$

The solution of this NLP is then an implicit function of $\mathbf{p}$. The optimal solution for a marginal change in parameter values is often of interest. A first-order predictor of the optimal solution can approximate the solution for a change in $\mathbf{p}$ as

$$
\mathbf{w}(\mathbf{p} + \Delta\mathbf{p}) \approx \mathbf{w}(\mathbf{p}) + \frac{\partial \mathbf{w}}{\partial \mathbf{p}}\Delta\mathbf{p}.
\tag{2.15}
$$

This first-order approximation is locally valid as long as there are no changes in the active set $\mathcal{A}$. This predictor can for example be used in homotopy-path-following methods, as in this thesis.

2.2.4   Homotopy method

The principle of the homotopy method is based on the idea of using the existing optimal solution for a problem to find the solution for a slightly modified problem. If the modifications to the original problem are small, such that the optimal solution to the new problem is in the neighbourhood of the original solution, the homotopy method can be applied. Here, the homotopy method is used to generate the initial guess for a complex NLP (see Section 3.4.2) and to sweep through a set of parameters (see Paper B).

2.2.5   Numerical methods for inequality-constrained optimization

An NLP such as (2.10) that only has equality constraints can be solved by applying Newton's root-finding method to the nonlinear KKT conditions.

However, with inequality constraints, this becomes tricky due to the non-smooth complementarity conditions (2.13e). There are two known methods for treating such a problem: 1) the Interior Point (IP) method and 2) the Sequential Quadratic Programming (SQP) method. Because it requires relatively few function and gradient evaluations, the SQP method is widely used. IP methods have advantages for solving large-scale NLPs that involve many inequalities. Here, we use the IP method because the treated NLPs are large problems, and the applied open-source solver IPOPT is robust [24]. The IP method is presented in more detail below.

Interior Point (IP) method

Interior point methods aim to relax the non-smooth complementarity conditions by introducing the relaxation parameter (barrier parameter) $\tau > 0$. The relaxed KKT conditions are then formulated as

$$\nabla_{\mathbf{w}}\Phi(\mathbf{w}^\star) + \nabla_{\mathbf{w}}\mathbf{g}(\mathbf{w}^\star)\boldsymbol{\nu} + \nabla_{\mathbf{w}}\mathbf{h}(\mathbf{w}^\star)\boldsymbol{\mu} = 0 \tag{2.16a}$$

$$\mathbf{g}(\mathbf{w}^\star) = 0 \tag{2.16b}$$

$$\mathbf{h}(\mathbf{w}^\star) \leq 0 \tag{2.16c}$$

$$\boldsymbol{\mu}^\star \geq 0 \tag{2.16d}$$

$$\boldsymbol{\mu}_i^\star\,\mathbf{h}_i(\mathbf{w}^\star) + \tau = 0. \tag{2.16e}$$

The last equation describes a hyperbola that for very small τ delivers a very close approximation to the original L-shaped complementarity conditions, see Fig. 2.2.
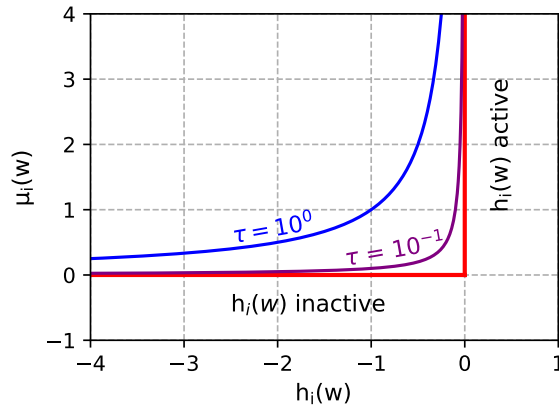
Figure 2.2: The non-smooth L-shaped manifold of the complementarity conditions in the KKT equations. In numerical methods, these conditions are relaxed via the barrier parameter τ. With $\tau \to 0$ the original problem is recovered.

Interior point methods normally initiate the problem with a large τ, e.g. 0.1, and solve the resulting system. Iteratively, the parameter τ is decreased to eventually recover a close approximation of the original problem. For each iteration, the previous solution is taken as an initial guess. In fact, this can be seen as a homotopy.

The problem (2.16) can be solved with the *primal* IP method or with the *primal-dual* IP method. The primal IP method takes the inequality constraint (2.16c) into the cost function Φ in the form of a barrier function. However, as τ approaches small values, the KKT conditions can become ill-conditioned and jeopardize convergence. This is not a problem in the PDIP method, which solves the relaxed KKT conditions as formulated in Eqs. (2.16).

Solving (2.16) with either the primal or the primal-dual IP method requires a feasible initial guess. Also, in order to ensure that $\mathbf{h}(\mathbf{w}) < 0$ holds, backtracking during Newton steps is required, which is costly if $\mathbf{h}$ is expensive. In order to solve these issues, slack variables $\mathbf{s}$ are introduced.

Slack formulation of primal-dual IP method

A slack variable $\mathbf{s}_i$ is introduced for each inequality constraint $\mathbf{h}_i$ such that

$$\nabla_{\mathbf{w}}\Phi(\mathbf{w}^\star) + \nabla_{\mathbf{w}}\mathbf{g}(\mathbf{w}^\star)\boldsymbol{\nu}^\star + \nabla_{\mathbf{w}}\mathbf{h}(\mathbf{w}^\star)\boldsymbol{\mu}^\star = 0 \tag{2.17a}$$

$$\mathbf{g}(\mathbf{w}^\star) = 0 \tag{2.17b}$$

$$\mathbf{h}_i(\mathbf{w}^\star) + \mathbf{s}_i^\star = 0 \tag{2.17c}$$

$$\mathbf{s}_i^\star\boldsymbol{\mu}_i^\star - \tau = 0 \tag{2.17d}$$

$$\boldsymbol{\mu}, \mathbf{s} \geq 0. \tag{2.17e}$$

At convergence, the condition of $\mathbf{h} \leq 0$ is now ensured by $\mathbf{s} \geq 0$, which is easier to enforce than the condition of $\mathbf{h} \leq 0$. With $\tau = 0$ the original KKT conditions are recovered. A widely known open-source solver for this method is IPOPT [24], which solves the problem (2.17) with Newton methods. IPOPT is used in this thesis.

In order to solve an LP of the form (2.11), the *simplex method* is widely used, cf. [25]. As no studies in this thesis focus on the mathematical background of that method, no details are presented here.

2.3 Optimal control

Combining optimization with dynamic systems leads us to the topic of optimal control. An Optimal Control Problem (OCP) aims to solve a dynamic system over time with respect to a cost functional Φ that is minimized. OCPs play a decisive role in this thesis, and this section introduces the concept of optimal control and presents important numerical methods.

The general formulation of an implicit OCP with DAE is given by

$$\min_{\mathbf{x}(.),\mathbf{u}(.)} \Phi(\mathbf{x}, z, \mathbf{p}) = E(\mathbf{x}(T), z(T), \mathbf{p}) + \int_0^T L(\mathbf{x}(t), z(t), \mathbf{u}(t), \mathbf{p}) \, dt \quad (2.18a)$$

$$\text{s.t.} \quad \mathbf{F}(t; \mathbf{x}(t), \dot{\mathbf{x}}(t), z(t), \mathbf{u}(t), \mathbf{p}) = 0, \qquad t \in [0, T] \quad (2.18b)$$

$$\mathbf{h}(\mathbf{x}(t), z(t), \mathbf{u}(t), \mathbf{p}) \leq 0, \qquad t \in [0, T] \quad (2.18c)$$

$$\mathbf{r}(\mathbf{x}(0), \mathbf{x}(T)) = 0, \qquad (2.18d)$$

where (2.18a) is the cost functional to be minimized, (2.18b) the system dynamics, (2.18c) the path constraints, and (2.18d) the boundary constraints. The functional (2.18a) is defined by the Lagrange term L under the integral, and a terminal cost E, also called the Mayer term.

Numerical approaches
There are three approaches to addressing an OCP as (2.18), via: 1) the "principal of optimality"; 2) indirect methods; and 3) direct methods.
The "principal of optimality" states that if a trajectory is optimal, each sub-arc of that trajectory is optimal, too. This principle is the basis for the continuous approach of the Hamilton-Jacobi-Bellman equation as well as for the discrete version of dynamic programming. This approach is mainly suitable for few-dimensional problems as it suffers from "the curse of dimensionality" [26].
The *indirect* methods are also known by the statement "first optimize, then discretize". These methods make use of the necessary conditions of optimality by formulating *Pontryagin's maximum principle* and generating a two-point boundary value problem that can be solved numerically by shooting or collocation techniques. These numerical techniques are detailed later. The major drawback is that problems with path constraints are difficult to handle.
The *direct* methods follow the principle of "first discretize, then optimize". These methods first transform the whole OCP into a discrete large-scale NLP. Unlike the indirect methods, direct methods are able to treat any kind of path constraints. Different direct methods exist that mainly differ in how they handle the state trajectories. For large constrained optimal control

problems, direct methods are nowadays the most successful approach and are therefore also used in this thesis. The NLPs in this thesis are solved with the direct collocation method, which is explained in the following section.

2.3.1 Direct optimal control

Direct methods follow the principle of "first discretize, then optimize". Thus, the infinite-dimensional control problem (2.18) is first discretized to a finite NLP. In principle, there are three direct methods: *direct single shooting*, *direct multiple shooting*, and *direct collocation*.

In the direct single shooting method, the control function is discretized to piecewise constant controls on a fixed time grid $[0, t_1, \ldots, T]$, such that $\mathbf{u}(t \in [t_k, t_{k+1}])$. The state trajectories $\mathbf{x}(t)$ are then functions of the discretized controls $\mathbf{w} = [\mathbf{u}_0, \ldots \mathbf{u}_{N-1}]$, the initial state $\mathbf{x}_0$, and the time t, such that $\mathbf{x}(t)$ can be obtained for the entire time grid $[0, T]$ via a forward integration of the system dynamics $\mathbf{F}$ (2.18b). Integration methods such as those discussed in Section 2.1.1 can be used. Direct single shooting is also known as the *sequential* approach, as integration and optimization are handled on different levels. However, direct single shooting can be problematic as difficulties arise when simulating nonlinear dynamics over a long time horizon.

As a solution to the problem of the long integration times, the multiple shooting method reduces the integration horizon for the system states by breaking down the time horizon $[0, T]$ into shorter integration intervals. Hence, multiple shooting only integrates over the time interval $[t_k, t_{k+1}]$ using the same piecewise constant controls as in the direct single shooting approach. Continuity constraints ensure that the final state of one interval matches the initial state of the next interval. With this method, long time horizons T can be handled.

In direct collocation, the states are discretized in an even finer grid than in multiple shooting, namely additionally on a collocation time grid within each time interval $[t_k, t_{k+1}]$. In each time interval, the states are then approximated by Lagrange polynomials, see Section 2.1.1 where the collocation integration method was introduced. In each time interval, the states are approximated via polynomials. Direct collocation handles the integration and optimization simultaneously and solves it all together in one large sparse NLP. Direct collocation is used in this thesis, because implicit functions are most easily handled with the collocation technique, and the exact Hessian is less computationally expensive to obtain than with the other approaches. The OCP (2.18) describes the dynamics implicitly and contains algebraic variables. A discretization of (2.18) via the direct collocation method results

in the following NLP

$$
\min_{\mathbf{w},\mathbf{z}} \quad \Phi(\mathbf{w},\mathbf{p})
$$

$$
\text{s.t.} \quad \mathbf{g}(\mathbf{w}) = \begin{bmatrix}
\mathbf{s}_0(\boldsymbol{\theta}_0, t_{0,0}) - \mathbf{x}_0 \\
\mathbf{s}_0(\boldsymbol{\theta}_0, t_{0,J}) - \mathbf{s}_1(\boldsymbol{\theta}_1, t_{1,0}) \\
\mathbf{F}(\mathbf{s}_0, \dot{\mathbf{s}}_0, \mathbf{u}_0, \mathbf{z}_0, \mathbf{p}) \\
\ldots \\
\mathbf{s}_k(\boldsymbol{\theta}_k, t_{k,J}) - \mathbf{s}_{k+1}(\boldsymbol{\theta}_{k+1}, t_{k+1,0}) \\
\mathbf{F}(\mathbf{s}_k, \dot{\mathbf{s}}_k, \mathbf{u}_k, \mathbf{z}_k, \mathbf{p}) \\
\ldots \\
\mathbf{s}_{N-2}(\boldsymbol{\theta}_{N-2}, t_{N-2,J}) - \mathbf{s}_{N-1}(\boldsymbol{\theta}_{N-1}, t_{N-1,0}) \\
\mathbf{F}(\mathbf{s}_{N-1}, \dot{\mathbf{s}}_{N-1}, \mathbf{u}_{N-1}, \mathbf{z}_{N-1}, \mathbf{p})
\end{bmatrix} = 0,
$$

$$
\mathbf{h}(\mathbf{w},\mathbf{p}) \leq 0,
$$

$$
\mathbf{r}\big(\mathbf{s}_0(\boldsymbol{\theta}_0, t_{0,0}), \mathbf{s}_{N-1}(\boldsymbol{\theta}_{N-1}, t_{N-1,J})\big) \leq 0,
$$

(2.19)

with the decision variables $\mathbf{w} = [\boldsymbol{\theta}_{0,1}, \ldots, \boldsymbol{\theta}_{0,J}, \mathbf{u}_0, \mathbf{z}_0, \ldots, \boldsymbol{\theta}_{N-1,J}, \mathbf{u}_{N-1}, \mathbf{z}_{N-1}]$. The state trajectory $\mathbf{s}_k(\boldsymbol{\theta}_k, t_k) = \boldsymbol{\theta}_k$ and the state derivatives $\dot{\mathbf{s}}_k(\boldsymbol{\theta}_k, t_k)$ in each interval $[k, k+1]$ are approximated with a Lagrange polynomial and its partial derivative, as introduced in Eq. (2.8). The equality constraints $\mathbf{g}$ collect the initial value constraint, the continuity conditions, and the collocation conditions, which principally are the integration constraints. The collocation conditions (i.e. the system dynamics $\mathbf{F}$) are enforced on each time step $t_{k,i}$, where $k \in \{0, 1, \ldots, N\}$ are the time intervals and $i = \{0, \ldots, J\}$ the indices of the collocation time points ψ_i. Here we use the Radau roots with a collocation degree of $J = 3$, resulting in the collocation time points of $\psi = \{0, 0.155051, 0.644949, 1\}$. Note that other conventions and collocation degrees can be chosen, and the values can be found in [23]. Constraints $\mathbf{h}(\cdot)$ and $\mathbf{r}(\cdot)$ are the path constraints and the boundary constraints, respectively. The NLP (2.19) is large and sparse and is solved by exploiting the sparse structure. This approach of handling all constraints simultaneously in one large NLP is also often called the *infeasible path* approach, because unlike the sequential approach, the state trajectories often remain infeasible until the NLP (2.19) is converged to an optimal solution.

In case of a parametric optimization, free parameters that are fixed over the entire optimization horizon are present as well. The "parameter dynamics" are then added to the above formulation with

$$
\mathbf{p}_{k+1} = \mathbf{p}_k \qquad k = 0, \ldots, N-1. \tag{2.20}
$$

The initial value $\mathbf{p}_0$ is not fixed, and thus $\mathbf{p}$ can be a time-independent parameter that is free for optimization. This way of implementing the parameters helps to preserve the sparse structure of the problem, which is exploited by the solver.

2.3.2 Free final time

In this thesis, a special case of a parametric OCP is handled, as a free final time is considered. This means that the final time T is an optimization parameter and since the number of discretization intervals is constant, the size of the time intervals $[t_k, t_{k+1}]$ varies during the solving process. This is handled by scaling the time instance in the collocation equations (2.19). The size of the finite elements is $h = \frac{1}{N}$. The dynamics are then scaled by

$$\mathbf{F}\left(\mathbf{s}_k, \dot{\mathbf{s}}_k \frac{1}{h \cdot T}, \mathbf{u}_k, z_k, \mathbf{p}\right) = 0, \tag{2.21}$$

so that the state trajectory and the collocation integration are dependent on the value of the final time T.

3

Power optimization of an AWE system

Unlike traditional wind turbines, an Airborne Wind Energy System (AWES) is able to adjust its operational altitude. Thus, the power generation of an AWES is not a function of the wind speed at a specific altitude. Instead, complex trade-offs have to be taken into account when computing the optimal power generation. Wind power grows cubically with the wind speed, and since wind speed generally increases with altitude, a long tether that allows for high flight seems beneficial for power generation. However, a longer tether increases the induced aerodynamic drag during flight and limits power generation. Also, for some weather phenomena and some locations, wind speeds do not necessarily increase with altitude and may form wind maxima at arbitrary altitudes. At the same time, crosswind kites produce the greatest lift with an orthogonal orientation to the wind vector, as is the case for the rotors of traditional horizontal-axis wind turbines. Consequently, the elevation angle of the tethered wing should be kept as low as possible.

This trade-off in operation altitude motivates the formulation of an OCP, a common approach within the AWE community to research control- and power-related questions [27–31]. Other work has proposed less complex quasi-steady state AWE models that predefine the flight trajectory and optimize power generation at specific discretized points [32]. For quick estimations of generated power, the analytical model of Loyd [10] can be used as done in [33].

In this thesis, the approach of formulating a detailed dynamic model in the form of an OCP is found to be the most practical choice. It allows for the study of the maximal power generation and optimal trajectory for different AWESs in varying wind conditions. To pursue a variety of research ques-

tions, the OCP formulation allows the optimization variables, parameters, and the objective functional to be varied.

This chapter includes the description of the mathematical model and the implementation in the optimal control framework. The first section presents the system dynamics, followed by a second section that describes the choice of system parameters. The third section presents a study on the model validation. Section 4 formulates the OCP. The last section presents the large-scale wind data used in this thesis.

In the following, vectors are denoted with bold lowercase letters ($\mathbf{x}$), matrices with bold uppercase ($\mathbf{X}$), and scalars with regular lowercase and uppercase letters (x, X). Functions are given with regular lowercase and uppercase letters as dependent on other variables ($x(\cdot)$, $X(\cdot)$).

3.1   Mathematical model of AWE system dynamics

The AWE model dynamics can be split into three parts: the rigid wing dynamics including a tether, the wind dynamics, and the interconnecting aerodynamics. The system and reference frames are illustrated in Fig. 3.1. Here, a drag-mode system is shown, but the same reference frames and parameter definitions hold for the modelled pumping-mode system.

The AWE systems in this thesis are assumed to consist of a rigid wing, modelled as a point mass with six degrees of freedom. The model is described in the Cartesian coordinate system using two reference frames: an Earth frame $\hat{n}$; and a body frame $\hat{b}$ that has its origin in the center of mass of the wing. The main wind direction is assumed to always be along the x-axis. The aerodynamics of the wing may be seen as the connecting link between the wind and the body dynamics. Below, the three model parts are presented and model choices discussed.

3.1.1   Rigid wing dynamics

The wing dynamics of the AWES describe the motion of the wing, which presents a flight trajectory that can evolve over a sphere that is centered at the ground attachment point of the tether. Many AWE models are based on minimal coordinates, with the 3-D positions of the wing described in Euler angles [34]. However, this approach also has disadvantages: 1) the projection of the body's velocity relative to the Earth frame entails complex and non-linear transformations; and 2) the formulation with Euler angles bears the risk of singularities. This latter issue implies a loss of one dimension, which

Figure 3.1: Illustration of the modelled wing with wing span c, chord b, and approximated wing area $S \approx c \cdot b$. A tether connects the center of the Earth frame $\hat{n}$ (ground station) to the center of mass (CoM) of the wing, which is the center of the body frame $\hat{b}$. The main wind direction is aligned with the x-axis of the Earth frame. Here, the electricity is generated onboard and transferred via the tether to the ground station. The pumping-mode system differs in how power is generated, with the tether being reeled out and generating rotational energy at a ground-based drum.

mathematically implies a rank deficiency of the matrix that relates the angular velocity vector to the time derivatives of the Euler angles. In practice this is also known as the "gimbal lock". Thus, even though the formulation of dynamics in minimal coordinates might be straightforward, the resulting mathematical model becomes complex and strongly nonlinear [27]. In this thesis, the model is mainly to be used for numerical optimal control, which preferably avoids highly nonlinear expressions or rotations that could end in a singularity point. That point or even being close to that point ought to be avoided in numerical optimization as it can jeopardize the convergence of the solver and hence the finding of the optimal solution. For these reasons, we choose a Cartesian coordinate system for the modelling.

The tether that connects the AWE wing with the ground station experiences full tension during power generation and can therefore be construed as a rigid rod, which is best treated via an algebraic constraint [27]. This holds for both pumping-mode and drag-mode systems.

The mathematical model is thus formulated in non-minimal coordinates, resulting in index-3 Differential Algebraic Equations (DAEs). The DAEs are reduced to index-1 in order to be able to apply traditional numerical inte-

gration methods. The equations are obtained from the dynamics described with Lagrangian mechanics and the algebraic constraint, presented below. For the rotations, a Direct Cosine Matrix (DCM) is used, which introduces nine individual decision variables but presents a less nonlinear and more stable transformation between the reference frames than other choices. The lower complexity and lower non-linearity of the model are well-suited for Newton-based optimal control methods.

Next, we describe the model dynamics based on the Lagrangian mechanics and the algebraic constraint, starting with the tether description. The tether connects the wing's CoM to the origin of the Earth frame. This connection enters the dynamics as a holonomic (purely position-dependent) algebraic constraint. The tether constraint is

$$c(\mathbf{q}) = \frac{1}{2}(\mathbf{q}^\top \mathbf{q} - \ell^2) = 0, \tag{3.1}$$

where $\mathbf{q} = [\mathbf{q}_x, \mathbf{q}_y, \mathbf{q}_z]$ is the position of the wing in natural coordinates and ℓ the tether length. The Lagrange function of the system is formulated as

$$\mathscr{L}(\mathbf{q}, \dot{\mathbf{q}}, \lambda) = \frac{1}{2}m\dot{\mathbf{q}}^\top \dot{\mathbf{q}} - mg\mathbf{q}_z - \frac{1}{2}\lambda(\mathbf{q}^\top \mathbf{q} - \ell^2). \tag{3.2}$$

By taking the time derivative of the constraint (3.1) twice, we obtain

$$\ddot{c}(\mathbf{q}, \dot{\mathbf{q}}, \ddot{\mathbf{q}}) = \mathbf{q}^\top \ddot{\mathbf{q}} + \dot{\mathbf{q}}^\top \dot{\mathbf{q}} - \dot{\ell}^2 - \ell\ddot{\ell}. \tag{3.3}$$

The system dynamics are then defined by

$$\frac{d}{dt}\frac{\partial \mathscr{L}}{\partial \dot{\mathbf{q}}} - \frac{\partial \mathscr{L}}{\partial \mathbf{q}} = \mathbf{f}, \quad \ddot{c}(\cdot) = 0, \tag{3.4}$$

leading to the basic translational dynamics of the model

$$\begin{bmatrix} m\,\mathbf{I}_3 & \mathbf{q} \\ \mathbf{q}^\top & 0 \end{bmatrix} \begin{bmatrix} \ddot{\mathbf{q}} \\ \lambda \end{bmatrix} = \begin{bmatrix} \mathbf{f} - mg\mathbf{q}_z \\ -\dot{\mathbf{q}}^\top \dot{\mathbf{q}} + \dot{\ell}^2 + \ell\ddot{\ell} \end{bmatrix}. \tag{3.5}$$

The external forces $\mathbf{f}$ are a summation of the aerodynamic forces $\mathbf{f}_A$ and the tether drag $\mathbf{f}_{\mathrm{Tdrag}}$, both detailed later. The expression $mg\mathbf{q}_z$ describes the gravitational force $\mathbf{f}_g$, which only has a z-component.

The rotational motion of the wing is defined by the DCM and its time evolution, describing the transformation vectors from the body frame $\hat{b}$ to the fixed Earth frame $\hat{n}$. The DCM can be decomposed into its columns, describing the longitudinal, transversal, and vertical axes of the wing in the body frame as $\mathbf{R} = [\mathbf{b}_x, \mathbf{b}_y, \mathbf{b}_z] \in \mathbb{R}^{3\times3}$. The time evolution of this rotation matrix is defined by

$$\dot{\mathbf{R}} = \mathbf{R}\boldsymbol{\omega}_\times, \tag{3.6}$$

where $\boldsymbol{\omega}_\times$ is the skew-symmetric matrix of the rotational angular velocities $\boldsymbol{\omega} \in \mathbb{R}^3$. The dynamics of the angular velocity depend on the inertia matrix $\mathbf{J}$ and the aerodynamic moments $\mathbf{m}_A$ and are described in the body frame as

$$\dot{\boldsymbol{\omega}} = \mathbf{J}^{-1} \left[\mathbf{m}_A - (\boldsymbol{\omega} \times \mathbf{J} \cdot \boldsymbol{\omega}) \right]. \tag{3.7}$$

The complete dynamics are then described by Eqs. (3.3),(3.5), (3.6), (3.7). We will return to these when we present the complete system model in Section 3.1.4.

3.1.2   Wind model

The wind is an essential part of the system environment, influencing the motion of the wing and eventually the instantaneous power output of the AWES. The wind speed is a function of the altitude, here referred to as the *wind profile*. In this model, the wind is aligned with the x-axis of the Earth frame, as visualized above in Fig. 3.1. We use two different types of wind profiles: 1) the commonly used power law [35]; and 2) polynomial functions that approximate real wind profiles. The wind speed function based on the power law (used in Paper C) is formulated as

$$\boldsymbol{w}_x(\mathbf{q}) = \mathrm{w}_0 \left(- \frac{\mathbf{q}_z}{h_0} \right)^{z_0}, \quad \boldsymbol{w}_y(\mathbf{q}) = \boldsymbol{w}_z(\mathbf{q}) = 0, \tag{3.8}$$

where $\boldsymbol{w} = [\boldsymbol{w}_x, \boldsymbol{w}_y, \boldsymbol{w}_z]$ denotes the three-dimensional wind speed, w_0 the reference wind speed at the reference altitude h_0, and z_0 the roughness length, defining the roughness of the terrain and thus influencing the shape of the wind profile. The variable $\mathbf{q}_z$ denotes the instantaneous altitude of the wing. Note that z is defined downwards, which is the reason for the negative vertical position. This representation of the wind profile is widely used to approximate wind speeds up to an altitude of around $100\,\mathrm{m}$.

In Papers B, D, E, the wind profiles are based on wind data obtained from reanalysis models, such as MERRA2 [36] and ERA5 [37]. This presents more realistic profiles and allows for the use of time- and location-determined wind data. The data are then processed so that the wind speed is expressed as a polynomial function of the altitude $\mathbf{q}_z$. The exact structure of the polynomials is described below in Section 3.5.1. The vertical wind component (z-axis) is neglected so that at each altitude the wind is represented in fact as a two dimensional vector.

Looking at the entire system, there is a feedback included as the wind speed influences the wing aerodynamic forces and moments $\mathbf{f}_A, \mathbf{m}_A$, which in turn affects the wing's translational and rotational accelerations ($\ddot{\mathbf{q}}, \dot{\boldsymbol{\omega}}$).

3.1.3 Aerodynamic model

The aerodynamics of the wing are an essential part as they describe how the motion of the air affects the motions of the rigid wing. The aerodynamics are wing specific, as the effects vary with the geometry of the wing. In this thesis, we assume that the airflow around the wing instantaneously settles into its steady state, so that the aerodynamic forces and moments depend on the instantaneous state only. The aerodynamics are determined by the aerodynamic forces and moments that act on the wing. The aerodynamic moments $\mathbf{m}_A$ consist of the roll, pitch, and yaw of the wing. The aerodynamic forces $\mathbf{f}_A$ consist of the drag, crosswind, and lift forces, acting parallel and perpendicular to the incoming airflow. The drag and lift forces are most essential to the flight behaviour, determining the forward and upward motion of the wing.

The forces and moments vary with the incoming airflow, the direction of which is defined by the angle of attack α and the side-slip angle β. These quantities are controlled via the surface deflections of the wing, namely aileron, elevator, and rudder, which are collected in the control inputs $\boldsymbol{\phi} = [\phi_a, \phi_e, \phi_r] \in \mathbb{R}^3$. An illustration of the mentioned terms can be seen in Fig. 3.2.

The negative airflow corresponds to the apparent wing velocity $\mathbf{v}_a$, which describes the difference between the wing velocity vector and the wind vector. The apparent wing velocity is mathematically described in the Earth frame as

$$\mathbf{v}_a = \dot{\mathbf{q}} - \boldsymbol{w}. \tag{3.9}$$

The resulting angle of attack α and side-slip angle β are expressed in radians in the body frame and are in the model approximated as

$$\alpha = -\frac{\hat{\mathbf{b}}_z^\top \mathbf{v}_a}{\hat{\mathbf{b}}_x^\top \mathbf{v}_a}, \qquad \beta = \frac{\hat{\mathbf{b}}_y^\top \mathbf{v}_a}{\hat{\mathbf{b}}_x^\top \mathbf{v}_a}. \tag{3.10}$$

The aerodynamic forces and moments are defined in the Earth frame and body frame, respectively, as

$$\mathbf{f}_a = \frac{1}{2}\rho \|\mathbf{v}_a\|^2 S \, \mathbf{R} \begin{bmatrix} C_X \\ C_Y \\ C_Z \end{bmatrix} \tag{3.11a}$$

$$\mathbf{m}_A = \frac{1}{2}\rho \|\mathbf{v}_a\|^2 S \begin{bmatrix} b\,C_l \\ c\,C_m \\ b\,C_n \end{bmatrix}, \tag{3.11b}$$

where ρ is the air density, S the effective wing area, b the reference wing span, and c the reference cord length of the wing. The values of $C_{\{X,Y,Z\}}$,
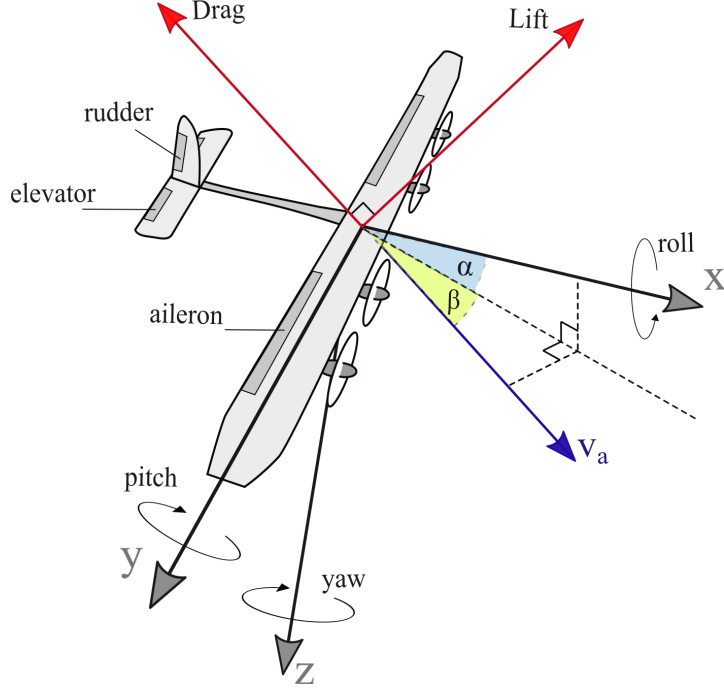
Figure 3.2: Illustration of the controls and respective moments on the wing. Lift and drag force directions are determined by the apparent wing velocity (negative airflow) $\mathbf{v}_a = \dot{\mathbf{q}} - \boldsymbol{w}$. The angles α and β denote the angle of attack (AoA) and the side-slip angle of the wing, respectively.

$C_{\{l,m,n\}}$ are the non-dimensional *aerodynamic coefficients*, commonly given in the body frame, and functions of $\mathbf{v}_a$, α, and β. Here, the moments $\mathbf{m}_A$ are kept in the body frame, while the forces $\mathbf{f}_a$ are transformed into the Earth frame via the rotation matrix $\mathbf{R}$. The choice of frames is linked to the way the dynamics of $\ddot{\mathbf{q}}$ and $\boldsymbol{\omega}$ are described in Eqs. (3.5) and (3.7). The force coefficients $C_{\{X,Y,Z\}}$ refer to the drag, crosswind, and lift coefficients, respectively. The moment coefficients $C_{\{l,m,n\}}$ mainly link the impact of the control surfaces on the rotational moments.

One of the main differences between a conventional and a tethered wing is the presence of the tether. Here, the tether is assumed to be attached at the CoM of the wing, so that no additional moments are generated by the tether. The general tether drag is defined in the Earth frame as

$$\mathbf{f}_{\text{Tdrag}} = -T_D \mathbf{v}_a, \tag{3.12}$$

where T_D is defined as in [38] as

$$T_{\text{D}} = \frac{1}{8} \rho \, C_{\text{T}} \, d_{\text{tet}} \, \ell \, \|\mathbf{v}_a\|, \tag{3.13}$$

with C_{T} as the drag coefficient of the tether and d_{tet} the tether diameter.

3.1.4 Power generation and complete model presentation

The aim of an AWES is to fly a trajectory that yields maximum power output. The power is generated differently for the two different kinds of AWE systems, pumping and drag mode. In the pumping-mode system, the lift force acting on the wing is used to reel out the tether from the winch, translating to rotational energy of a ground generator. In the drag-mode system, onboard propellers produce electricity during fast crosswind flights with the tether length kept constant ($\dot{\ell} = 0$). In the mathematical model, these two modes of power generation are expressed as

$$P = \begin{cases} \mathbf{f}_\text{t} \cdot \dot{\ell} = \lambda \cdot \mathbf{q} \cdot \dot{\ell} & \text{in lift mode,} & \text{(3.14a)} \\[2ex] \text{f}_\text{prop} \mathbf{v}_\text{a} \dfrac{\mathbf{v}_\text{a}}{\|\mathbf{v}_\text{a}\|} \, \eta_\text{tot} & \text{in drag mode.} & \text{(3.14b)} \end{cases}$$

Eq. (3.14a) describes the mechanical power obtained by the tether speed and the tether force, given by the Lagrange function (3.5) of the model dynamics. Here, mechanical energy is modelled, and no efficiency factor is considered. In Eq. (3.14b) the propeller dynamics and the resulting power generation are simplified and represented by a mechanical braking force f_prop. The force is aligned with the instantaneous direction of the apparent wing velocity $\mathbf{v_a}$. The efficiency η_tot includes both the factor representing how much thrust power can be transformed into propeller motion and the generator efficiency. The efficiency factor includes the transformation to electrical energy produced, which is required for the performed energy system studies. In the model, the force f_prop is implemented as a control input determining how much brake force is applied to the onboard generators and hence controlling how much power is generated.

Complete model
Finally, in order to deliver the complete dynamic model all at once, the model equations (3.3), (3.5), (3.6), (3.7), and (3.14) are brought together to yield the complete system dynamics $\mathbf{F}_\text{sys}$:

$$\begin{aligned} \dot{\mathbf{q}} &= \mathbf{v} \\ \ddot{\mathbf{q}} = \dot{\mathbf{v}} &= m^{-1} \left[\mathbf{f}_\text{A} + \mathbf{f}_\text{g} + \mathbf{f}_\text{Tdrag} + \mathbf{f}_\text{t} \right] \\ 0 &= \mathbf{q}^\top \ddot{\mathbf{q}} + \dot{\mathbf{q}}^\top \dot{\mathbf{q}} - \dot{\ell}^2 - \ell\ddot{\ell} \\ \dot{\mathbf{R}} &= \mathbf{R}\boldsymbol{\omega}_\times \\ \dot{\boldsymbol{\omega}} &= \mathbf{J}^{-1} \left[\mathbf{m}_\text{A} - (\boldsymbol{\omega} \times \mathbf{J} \cdot \boldsymbol{\omega}) \right] \\ \dot{E} &= P. \end{aligned} \qquad (3.15)$$

Collecting the system differential and algebraic states as $\mathbf{x}$, $\mathbf{z}$, and the control inputs $\mathbf{u}$ results in

$$
\mathbf{x} = \begin{bmatrix} \mathbf{q} \\ \mathbf{v} \\ \mathbf{r} \\ \boldsymbol{\omega} \\ \ell \\ \dot{\ell} \\ \boldsymbol{\phi} \\ E \end{bmatrix} \in \mathbb{R}^{24}, \qquad z = \lambda \in \mathbb{R}, \qquad \mathbf{u} = \begin{bmatrix} \dot{\boldsymbol{\phi}} \\ \ddot{\ell} \\ \mathrm{f_{prop}} \end{bmatrix} \in \mathbb{R}^{4}. \qquad (3.16)
$$

The differential states $\mathbf{x}$ include the position $\mathbf{q} \in \mathbb{R}^3$, the velocity $\mathbf{v} \in \mathbb{R}^3$, the rotation vector $\mathbf{r} \in \mathbb{R}^9$, the angular velocity $\boldsymbol{\omega} \in \mathbb{R}^3$, the tether length $\ell \in \mathbb{R}$, the tether velocity $\dot{\ell} \in \mathbb{R}$, the controls $\Phi \in \mathbb{R}^3$, and the energy $E \in \mathbb{R}$. The rotation vector $\mathbf{r}$ contains the entries of the rotation matrix $\mathbf{R}$. The algebraic variable z is connected to the algebraic tether constraint. The control inputs $\mathbf{u}$ collect the time derivative of the surface controls $\dot{\boldsymbol{\phi}} \in \mathbb{R}^3$, the tether acceleration $\ddot{\ell} \in \mathbb{R}$, and the onboard propeller braking force $\mathrm{f_{prop}} \in \mathbb{R}$.

The system can be used for both modelling the drag-mode and the lift-mode AWES by setting not-used variables to zero and including the correct power production function. In the drag-mode case, the tether length is constant, i.e. $\dot{\ell} = \ddot{\ell} = 0$. In the lift-mode case, the AWES has no onboard propeller, so $\mathrm{f_{prop}} = 0$.

3.2 Model data

The following sections present the model data used in the studies. The aerodynamic coefficient equations are detailed, followed by the numerical values of the wing parameters. Both parts have a first paragraph on the pumping-mode wing modelled in Paper A and a second paragraph about the wing modelled in the studies presented in Papers B, D, and E.

3.2.1 Aerodynamic coefficients

The aerodynamic coefficients of a wing are essential parameters, determined by the design and influencing the performance of a wing. The main factors of the wing aerodynamics are lift and drag forces, which are connected to the force coefficients C_Z and C_X. They are also commonly known as the lift coefficient $C_L = -C_Z$ and the drag coefficient $C_D = -C_X$. In general, high

lift and low drag are preferred in order to obtain a high glide ratio and a large lift during flight. The drag consists of the parasitic drag, which increases with the angle of attack, and the lift-induced drag, which decreases with the angle of attack. The total drag force results in a U-shaped drag curve. The lift is almost linearly increasing with the angle of attack, up to a designed maximum. Beyond that point, the aircraft eventually stalls due to flow separation on the wing. In aerospace engineering, the lift-over-drag (LoD) ratio is an important wing design aspect. In the field of AWE, the ratio of C_L^3/C_D^2 is also a decisive factor. A wing with a high C_L^3/C_D^2 provides a high tether tension, which is preferable for a high power output [10].

Choice of aerodynamic coefficients
In this thesis, different aerodynamic coefficients have been used for different studies. In a validation study of the pumping-mode model, a detailed aerodynamic model has been provided by the company Ampyx power [1] and is implemented in the AWE model. In the remaining work, the aerodynamic coefficients are approximated for large-scale drag-mode systems.
For the AWE model validation, the simulated state trajectories are compared to flight measurements for a pumping-mode prototype wing. Here, the aerodynamic model has been available from Ampyx power [1]. The coefficients are given as series expansions, showing dependencies on the instantaneous states of $\boldsymbol{\omega}$, $\mathbf{v}_a$, α, β, and controls $\boldsymbol{\phi}$ as

$$
\begin{bmatrix} C_X \\ C_Y \\ C_Z \end{bmatrix} = \begin{bmatrix} C_{X0}(\alpha) \\ C_{Y0}(\alpha) \\ C_{Z0}(\alpha) \end{bmatrix} + \begin{bmatrix} C_{X\beta}(\alpha) \\ C_{Y\beta}(\alpha) \\ C_{Z\beta}(\alpha) \end{bmatrix} \beta
$$
$$
+ \begin{bmatrix} C_{Xp}(\alpha) & C_{Xq}(\alpha) & C_{Xr}(\alpha) \\ C_{Yp}(\alpha) & C_{Yq}(\alpha) & C_{Yr}(\alpha) \\ C_{Zp}(\alpha) & C_{Zq}(\alpha) & C_{Zr}(\alpha) \end{bmatrix} \begin{bmatrix} b\,\omega_x \\ c\,\omega_y \\ b\,\omega_z \end{bmatrix} \frac{1}{2\|\mathbf{v}_a\|} \qquad (3.17)
$$
$$
+ \sum_{i\in\{a,e,r\}} \begin{bmatrix} C_{X\phi_i}(\alpha)\,\phi_i \\ C_{Y\phi_i}(\alpha)\,\phi_i \\ C_{Z\phi_i}(\alpha)\,\phi_i \end{bmatrix},
$$

and

$$
\begin{bmatrix} C_l \\ C_m \\ C_n \end{bmatrix} = \begin{bmatrix} C_{l0}(\alpha) \\ C_{m0}(\alpha) \\ C_{n0}(\alpha) \end{bmatrix} + \begin{bmatrix} C_{l\beta}(\alpha) \\ C_{m\beta}(\alpha) \\ C_{n\beta}(\alpha) \end{bmatrix} \beta
$$
$$
+ \begin{bmatrix} C_{lp}(\alpha) & C_{lq}(\alpha) & C_{lr}(\alpha) \\ C_{mp}(\alpha) & C_{mq}(\alpha) & C_{mr}(\alpha) \\ C_{np}(\alpha) & C_{nq}(\alpha) & C_{nr}(\alpha) \end{bmatrix} \begin{bmatrix} b\,\omega_x \\ c\,\omega_y \\ b\,\omega_z \end{bmatrix} \frac{1}{2\|\mathbf{v}_a\|} \qquad (3.18)
$$
$$
+ \sum_{i\in\{a,e,r\}} \begin{bmatrix} C_{l\phi_i}(\alpha)\,\phi_i \\ C_{m\phi_i}(\alpha)\,\phi_i \\ C_{n\phi_i}(\alpha)\,\phi_i \end{bmatrix},
$$

where the coefficients C_{ij}, with $i = \{X, Y, Z, l, m, n\}$, $j = \{0, \beta, p, q, r, \phi\}$, determine the dimensionless *aerodynamic derivatives*. The aerodynamic deriva-

tives are retrieved from the physical wing by a combination of flight tests, wind tunnel experiments, and CFD analyses. They are usually presented in look-up tables as dependencies of flight parameters as controls, angle of attack, and side-slip angles. However, look-up tables are not suitable for numerical simulations using gradient-based methods. Thus, the individual aerodynamic derivatives C. are interpolated to polynomial functions of α. The resulting numerical values for the polynomial parameters are given below in Table 3.2 in Section 3.2.2. The validation study is presented in Section 3.3.

For the remaining thesis work, the numerical values for such a detailed aerodynamic model have not been available. Thus, Eq. (3.17) is approximated using the classical lifting-line theory of Prandtl [39] as well as internal company information. Applying this theory to the AWE wing results in a lift coefficient C_L and a drag coefficient C_D, which both depend on the angle of attack α and side-slip angle β. The crosswind force is determined by the drag C_Y, which is mainly generated by the pylons that carry the propellers in the drag-mode system. The three force coefficients are then given as

$$
\begin{aligned}
C_L &= C_{L0} + 2\pi \frac{\mathit{AR}}{2 + \mathit{AR}}\, \alpha \\
&= C_{Z,0,0} + C_{Z,0,1}\, \alpha = \text{-}C_Z \\
C_D &= C_{D0} + \frac{C_L^2}{\pi\, e\, \mathit{AR}} + n_p C_Y + n_p C_Y^2 \frac{1}{\pi \mathit{AR}_p} \frac{S_p}{S} \\
&= C_{X,0,0} + C_{X,0,2}\, \alpha^2 + C_{X,\beta^2}\, \beta^2 = \text{-}C_X \\
C_Y &= -2\pi \frac{\mathit{AR}_p}{2 + \mathit{AR}_p} \beta = C_{Y\beta}\, \beta,
\end{aligned}
\tag{3.19}
$$

where $e = 1$ determines the elliptical wing profile, n_p the number of pylons, and AR and AR_p determine the aspect ratios of wing and pylons, respectively. The moment coefficients depend on the wing shape and the wing inertia matrix and are modelled as a simplification of Eq. (3.18):

$$
\begin{aligned}
\begin{bmatrix} C_l \\ C_m \\ C_n \end{bmatrix} &= \begin{bmatrix} C_{lp}(\alpha) & 0 & C_{lr}(\alpha) \\ 0 & C_{mq}(\alpha) & 0 \\ C_{np}(\alpha) & 0 & C_{nr}(\alpha) \end{bmatrix} \begin{bmatrix} b\,\omega_x \\ c\,\omega_y \\ b\,\omega_z \end{bmatrix} \frac{1}{2\|\mathbf{v}_a\|} \\
&\quad + \sum_{i \in \{a,e,r\}} \begin{bmatrix} C_{l\phi_i}(\alpha)\,\phi_i \\ C_{m\phi_i}(\alpha)\,\phi_i \\ C_{n\phi_i}(\alpha)\,\phi_i \end{bmatrix}.
\end{aligned}
\tag{3.20}
$$

3.2.2 Wing parameters

This section gives the data for the modelled pumping-mode and drag-mode systems used in the studies. Numerical values related to the wing-shape and corresponding aerodynamic coefficients are listed.

Pumping-mode system (Paper A)

In Paper A, the AWES model is validated against flight data of the pumping-mode system of Ampyx Power [1], and thus the wing and tether parameters as well as the aerodynamic coefficients are aligned to their prototype AP2. The aerodynamic model presented in Eqs. (3.17) and (3.18) are used with the wing and tether parameters listed in Table 3.1.

Table 3.1: Kinematic and geometric system specifications of the Ampyx wing AP2. These values are used for the model validation, which is described in Section 3.3 and published in Paper A.

parameter	value	description
S	3	wing area [m^2]
b	5.5	wing span [m]
c	0.55	wing chord [m]
m	36.8	weight [kg]
$J_{(xx,yy,zz,xz)}$	25, 32, 56, -0.47	inertia matrix [kg·m^2]
d_{tet}	0.0025	tether diameter [m]
ρ_t	0.0046	tether density [kg/m]
C_t	1.2	tether drag coefficient [-]
ρ	1.225	air density [kg/m^3]

The aerodynamic coefficients were obtained in flight tests and CFD simulations. The aerodynamic derivatives of Eqs. (3.17), (3.18) are interpolated to polynomial functions of α. The resulting polynomial parameters are given in Table 3.2, listed as $[c_2\,c_1\,c_0]$, so that the aerodynamic coefficients for the model given by (3.17) and (3.18) are obtained as

$$C_. = \begin{bmatrix} c_2 & c_1 & c_0 \end{bmatrix} \begin{bmatrix} \alpha^2 \\ \alpha \\ 1 \end{bmatrix}. \tag{3.21}$$

Parameters that are not listed are equal to zero.

Drag-mode system (Papers B, D, E)

In Papers B,D, and E, different drag-mode systems are modelled with the aim of comparing their power generation to the power generated by a traditional wind turbine. For this comparison, we model an AWES with a large wing rated at a capacity of 2 MW, the standard size of current wind turbines. Such a wing is relatively heavy and requires a thick tether for transferring 2 MW, which affects the flight behaviour. As an alternative, we

Table 3.2: Dimensionless polynomial derivatives resulting in the aerodynamic coefficients, using Eq. (3.21).

C_X	value	C_m	value
C_{X_0}	[2.5549, 0.4784, -0.0293]	C_{m_0}	[0,-0.6027, -0.0307]
C_{X_q}	[0, 4.4124, -0.6029]	C_{m_q}	[5.2885,-0.0026,-11.3022]
$C_{X_{\phi_e}}$	[0, 0.1115,-0.0106]	$C_{m_{\phi_e}}$	[0.9974,-0.0061,-1.0427]
		$C_{m_{\phi_r}}$	[0,0,-0.0015]
C_Y		**C_l**	
C_{Y_β}	[0.0936,-0.0299,-0.1855]	C_{l_β}	[0.0312,-0.0003 ,-0.0630]
C_{Y_p}	[0.0496,-0.0140,-0.1022]	C_{l_p}	[0.2813,-0.0247,-0.5632]
C_{Y_r}	[0,0.1368,0.1694]	C_{l_r}	[0,0.6448,0.1811]
$C_{Y_{\phi_a}}$	[0.0579,-0.0024,-0.0514]	$C_{l_{\phi_a}}$	[0.2383,-0.0087,-0.2489]
$C_{Y_{\phi_r}}$	[-0.1036,0.0268,0.10325]	$C_{l_{\phi_r}}$	[0,-0.0013,0.00436]
C_Z		**C_n**	
C_{Z_0}	[5.7736, -5.0676, -0.5526]	C_{n_β}	[0,-0.0849,0.0577]
C_{Z_q}	[6.1486,0.1251,-7.5560]	C_{n_p}	[0,-0.9137,-0.0565]
$C_{Z_{\phi_e}}$	[0.2923,-0.0013,-0.315]	C_{n_r}	[0.02570,0.0290,-0.0553]
		$C_{n_{\phi_a}}$	[0,-0.1147,0.01903]
		$C_{n_{\phi_r}}$	[0.04089,-0.0117,-0.0404]

also model smaller wings with a capacity of 666 kW. Installing three of this kind next to each other would also relate to a 2 MW system. This configuration takes larger ground space but shows different flight characteristics as, e.g. a lower cut-in wind speed, lower tether drag, and more hours of power generation at rated capacity. Here, a single 666 kW wing is modelled and the power is multiplied by three without considering wake losses or other power generation differences. Figure 3.3 shows the three system configurations modelled, the 2 MW wing, the wind turbine and the 3×666 kW system, which is used for comparison in Papers D and E. The power production of the wind turbine is modelled with a rotor diameter of 100 m and a generator size of 1.94 MW. More on the WT modelling can be found in the respective papers. The data for the two drag-mode systems modelled are in part obtained from the Makani prototypes and manuscripts [11, 40–42] and in part derived from internal company data. To date, the largest prototype tested is a 600 kW AWES built by Makani [11]. A prototype of 5 MW was planned. The respective wing values for these prototypes are used as a basis for the modelled systems. The AWES parameters for the small and the large wing are listed in Table 3.3. The wing and tether parameters, aspect ratio (Æ), tether length, mass, and wing span, are aligned to the Makani wings and adjusted to the capacity size that is modelled in the thesis. The param-

(a) 2 MW AWES

(b) 2 MW WT

(c) three aligned 666 kW AWESs
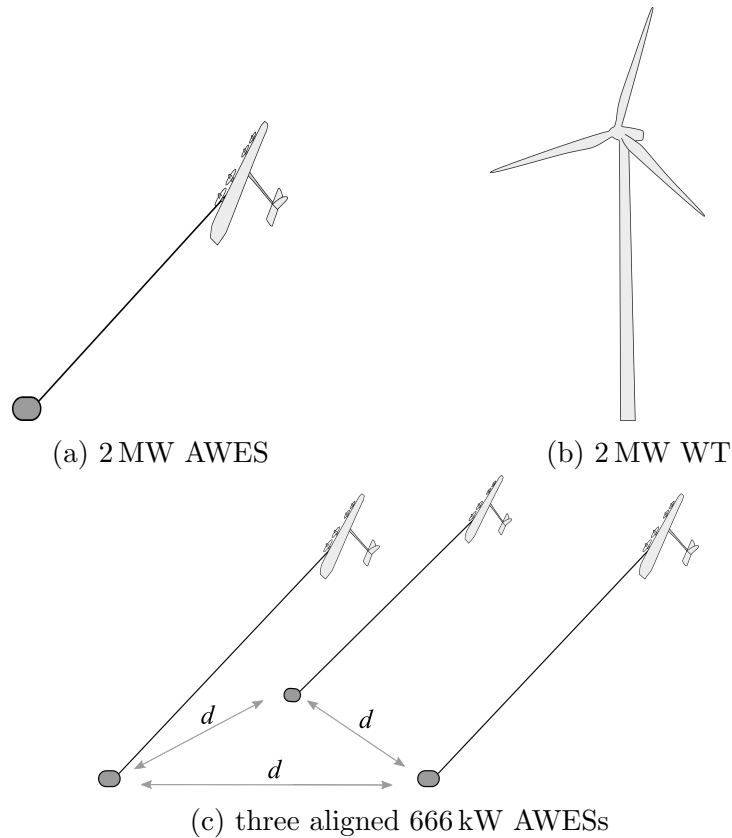
Figure 3.3: The three modelled wind power systems: a 2 MW AWES, a wind turbine, and three aligned smaller 666 kW AWESs. The distance d between the three smaller wings equals the modelled tether length of 500 m. Note that the relative proportions of the systems are not realistic.

eters of the smaller wing are taken from Makani's 0.6 MW system [40]. The parameters for the modelled 2 MW wing are interpolated from the data of Makani's 0.6 MW system and planned 5 MW wing. The tether diameter and power-related parameters are taken from [41], where tether dimensions are computed based on specific materials, power, and voltage levels. The here chosen generator capacity, voltage level, and aluminium conductor result in the tether diameters presented in Table 3.3. The aerodynamic coefficients for the wings are estimated from [42, 43] and are listed in Table 3.4. The resulting LoD curves are visualized in Fig. 3.4.

Table 3.3: Wing data for the two AWE systems modelled.

Parameter	small	large	description
P	0.666	2	rated power [MW]
S	36	70	surface [m^2]
b	28	40	wing span [m]
$\mathit{\!R}$	21.78	22.85	wing aspect ratio [-]
$\mathit{\!R}_p$	3.5	3.5	pylons aspect ratio [-]
m	1050	3000	wing mass [kg]
$J_{(xx,yy,zz)}$	$(2,1,2.5) \cdot 10^4$	$(24,1.7,20) \cdot 10^4$	inertia matrix [kg·m^2]
ℓ	500	500	tether length [m]
m_t	250	600	tether mass [kg]
d_{tet}	0.027	0.045	tether diameter [m]
V	5	5	voltage [kV]
η_{prop}	0.8	0.8	propeller efficiency [-]
η_{tet}	0.97	0.97	cable efficiency [-]
η_{tot}	0.75	0.75	total efficiency [-]
α_{max}	2	2	max. angle of attack[°]

Table 3.4: Aerodynamic derivatives for the drag-mode wing. Left: Force components for the large and small drag-mode system, respectively. Right: Moment components, which are the same for both systems. Vectors correspond to polynomial coefficients, using Eq. (3.21). Scalar values correspond to α-independent parameters.

Force components		
	large	small
$C_{\text{X},0}$	$[-0.23, 0, -0.06]$	$[-0.27, 0, -0.05]$
$C_{\text{Z},0}$	$[0, -5.78, -1.80]$	$[0, -5.75, -1.80]$
C_{X,β^2}	-0.33	-0.65
$C_{\text{Y},\beta}$	-4.00	-4.00

Moment components			
$C_{\text{m}0}$	-0.3	$C_{\text{n}p}$	-0.3
$C_{\text{n}\beta}$	0.2	$C_{\text{n}r}$	-0.03
$C_{\text{l}p}$	-0.7	$C_{\text{l}\phi_r}$	0.3
$C_{\text{l}r}$	0.5	$C_{\text{m}\phi_a}$	0.6
$C_{\text{m}q}$	-29.5	$C_{\text{n}\phi_e}$	0.2

3.3 Model validation

The mathematical model of the AWES approximates the wing dynamics as a point-mass model and the tether as a rigid rod. In order to analyse the validity of that model, formulated as $\mathbf{F}_{\text{sys}}$ (3.15), the modelled state trajectories are compared to real flight measurements from the Ampyx power prototype AP2 (Paper A). The model parameters, including aerodynamic coefficients and wing characteristics, equal the parameters of the prototype wing. The validation is conducted with a least-squares (LS) fitting problem. The LS problem minimizes the difference between the state trajectories and
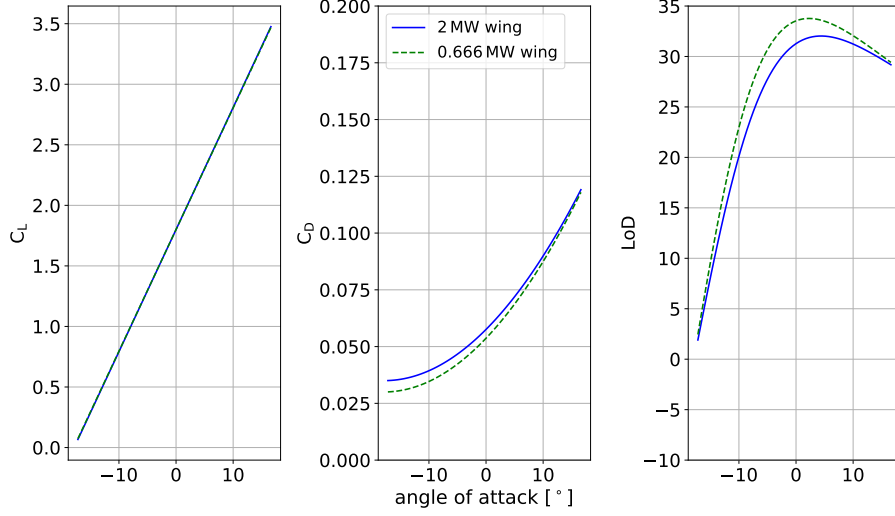
Figure 3.4: C_L, C_D, and LoD curve for the modelled large 2 MW and the smaller 0.666 MW drag-mode wing. At the maximal LoD values at $\alpha_{\max} = 2°$, $L^3/D^2 = 2027$ and 2280, for the large and the small wing, respectively.

the measurements as

$$\min_{\mathbf{y}} \quad \int_0^{t_f} (\mathbf{y} - \hat{\mathbf{y}})^\top W_{\mathbf{y}} (\mathbf{y} - \hat{\mathbf{y}}) + W_{\boldsymbol{w}} \|\dot{\boldsymbol{w}}\|^2 \, \mathrm{d}t$$

$$\text{s.t.} \qquad\qquad\qquad\qquad\qquad \mathbf{F}_{\text{sys}} = 0, \tag{3.22}$$

where $\mathbf{y}$ denotes the modelled states and $\hat{\mathbf{y}}$ the measured states. The states that are part of the state vector $\mathbf{y}$ are the position $\mathbf{q}$, velocity $\mathbf{v}$, the rotation matrix $\mathbf{R}$, the angular velocity $\boldsymbol{\omega}$, the tether speed $\dot{\ell}$, and the control inputs $\boldsymbol{\phi}$. In this validation study, the wind vector $\boldsymbol{w}$ is taken as part of the state, while its time derivative $\dot{\boldsymbol{w}}$ becomes a piecewise constant control input and can be described as a random walk driven by a Gaussian white noise. The vector $\hat{\mathbf{y}}$ includes the respective states as measurement data for one flight orbit. In the cost function, the input variable $\dot{\boldsymbol{w}}$ is minimized using a squared penalty. The weight matrix $W_{\mathbf{y}}$ and the scalar $W_{\boldsymbol{w}}$ comprise approximations of the covariance of the measurement noise and the wind rate of change, respectively. The minimization is constrained by the system dynamics $\mathbf{F}_{\text{sys}}$. The results show that the proposed AWES model $\mathbf{F}_{\text{sys}}$ of Eq. (3.15) is able to approximate the state trajectories of the real system accurately. The differences between simulation and data for tether speed (reel-in and -out), tether tension, and the resulting mechanical power are visualized in Fig. 3.5. Despite the simplified treatment of the dynamic tether as a rigid rod, tether tension and the resulting power generation match the measurements fairly well. The relative error in power estimation for one pumping cycle appears
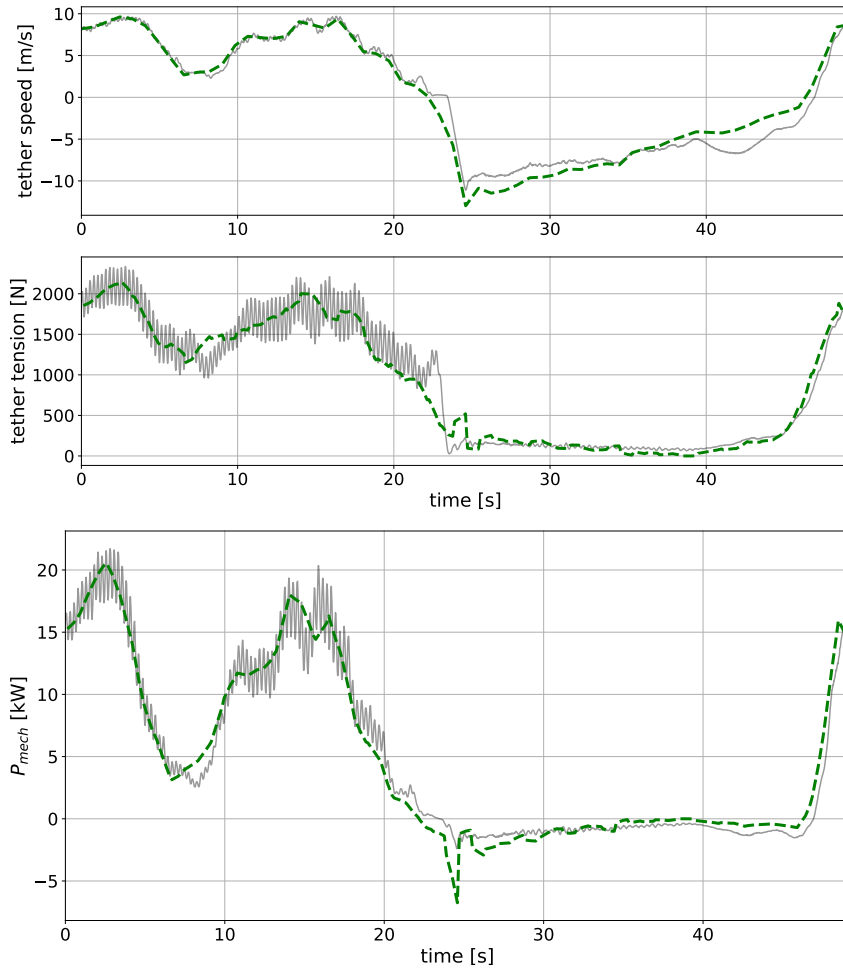
Figure 3.5: From top to bottom: Tether speed, tether tension, and mechanical power generated. The measured data are visualized in grey, while the simulated data are visualized in dashed green.

to be 0.92%. Note that the rigid tether approximation only holds during power generation (periodically flying orbits), when the tether is constantly under tension. Flight manoeuvres, i.e. launching and landing or adjusting to the wind alignment, can create slack in the tether, rendering the rigid-rod approximation not valid anymore. The research questions posed in this thesis pertain to AWES power generation, rather than to capturing various flight manoeuvres. Thus, the proposed model is found to be a valid choice and is used throughout this thesis. Validation results are presented in more detail in Paper A.

The presented model dynamics are only validated for the pumping-mode system. However, for the purposes of this thesis, we assume that the model is also a valid approximation for describing a drag-mode system.

3.4 Power optimization

The system model (3.15) described in Section 3.1.4 is built with the aim of studying the average power generation during a flight orbit. The optimal flight trajectory that results in the maximal power generation is a trade-off among several variables. The maximal tether force, and thus maximal power, is theoretically obtained at crosswind flight. However, as this is not realizable, an elevation angle of the wing of approximately 30° is common practice. However, the actual optimal elevation angle depends on the prevailing wind conditions. If the wind speed is constant across altitude, the optimal trajectory would be at as low altitude as possible. If the wind speeds are greater with increasing altitude, it might be beneficial to sacrifice the crosswind flight and increase the elevation angle.

To capture this trade-off and obtain the optimal trajectory for any wind conditions, the power computation is implemented as an optimization in an optimal control framework. The formulation of the OCP is described in the next section, followed by the explanation of how to retrieve an initial guess and how to solve the problem numerically.

3.4.1 OCP formulation and discretization

The average power during one cycle can be formulated either as an integral over the entire orbit time or as the energy at the final time as

$$\bar{P} = \frac{1}{T} \int_0^T P(t)\, dt = \frac{1}{T}\, E(T). \tag{3.23}$$

The OCP is then formulated as

$$\min_{\mathbf{x}, z, \mathbf{u}} \quad -\frac{1}{T}\, E(T) + \int_0^T \ell_{\text{Reg}}(\mathbf{u})\, \mathrm{d}t \tag{3.24a}$$

$$\text{s.t.} \quad \mathbf{F}(\dot{\mathbf{x}}, \mathbf{x}, z, \mathbf{u}, \mathbf{p}, T) = 0, \tag{3.24b}$$

$$\mathbf{c}(\mathbf{x}(0), \mathbf{x}(T)) = 0, \tag{3.24c}$$

$$\mathbf{h}(\mathbf{x}, z, \mathbf{u}, \mathbf{p}, T) \le 0. \tag{3.24d}$$

The power maximization enters the cost functional (3.24a) as a Mayer term. A Lagrange term adds a small regularization $\ell_{\text{Reg}}(\mathbf{u})$ that penalizes the control inputs $\mathbf{u}$. The constraint (3.24b) denotes the model dynamics (3.15). Constraint (3.24c) enforces the periodicity of the problem, and constraint (3.24d) gathers the actuator and operational limits of the system dynamics. Problem (3.24) is solved numerically using the *direct collocation method*, which belongs to the family of direct optimal control methods, described previously in Section 2.3.1. The problem is discretized to a finite-dimensional

NLP by splitting the state trajectories into N = 20 (alternatively N = {40,60}) control intervals. Within each control interval, the trajectories are represented by a Lagrange polynomial evaluated on the collocation points using a Radau scheme of degree 3. The numerical values of the collocation points can be found in [23]. The Radau scheme is chosen due to its good numerical stability in the presence of DAEs [23].

NLP of AWE power maximization

The direct collocation method collects all constraints concerning the system dynamics $\mathbf{F}(\cdot)$ (Eq. (3.15)) and the collocation constraints $\mathbf{G}(\cdot)$ in one large NLP as presented before in Eq. (2.19). The trivial kinematics of the system states and controls are added to the system dynamics as

$$\frac{d}{dt}\begin{bmatrix} \ell \\ \dot{\ell} \\ \phi \end{bmatrix} = \begin{bmatrix} \dot{\ell} \\ \ddot{\ell} \\ \dot{\phi} \end{bmatrix}. \tag{3.25}$$

The DAE for the tether constraints of Eq. (3.1) has been time-differentiated twice and is included in the system dynamics (3.15). The related consistency conditions $(c(\mathbf{q}) = 0$ and $\dot{c}(\mathbf{q}, \dot{\mathbf{q}}) = 0)$ have to be enforced at one time point, e.g. at t = 0. However, enforcing both leads to LICQ problems at the solution, such that only

$$0 = c(\mathbf{q}_0) = \frac{1}{2}(\mathbf{q_0}^\top \mathbf{q_0} - \ell_0^2) \tag{3.26}$$

is enforced [44].

This OCP describes a periodic problem by including the periodicity constraints (3.24c). However, simply enforcing $\mathbf{x}_0 = \mathbf{x}_N = 0$ leads to an over-constrained NLP and meaningless constraints like the periodicity of energy. The periodicity constraints $\mathbf{c}(\mathbf{x}_0, \mathbf{x}_N) = 0$ with the included states and controls are expressed as

$$[\boldsymbol{\omega}_0, \ell_0, \dot{\ell}_0, \boldsymbol{\phi}_0] = [\boldsymbol{\omega}_N, \ell_N, \dot{\ell}_N, \boldsymbol{\phi}_N] \tag{3.27}$$

$$\mathbf{u}_0 = \mathbf{u}_N. \tag{3.28}$$

To enforce both periodicity and orthogonality of the rotation matrix $\mathbf{R}$, we avoid over-constraining the problem by adding

$$0 = (\mathbf{R}(0)^\top \mathbf{R}(0) - \mathbf{I}_3)^\triangle \quad \text{and} \quad 0 = (\mathbf{R}(0)^\top \mathbf{R}(N) - \mathbf{I}_3)^\triangledown, \tag{3.29}$$

where $\triangle$ denotes the upper right triangle of the matrix, including the diagonal (six values) and $\triangledown$ the lower left triangle of the matrix (three values).

The periodicity constraints of the position and velocity are implemented with a lifting variable v_{lift} that is forced to zero as part of the cost function.

$$
\begin{aligned}
0 &= \mathbf{q}_0 - \mathbf{q}_N + v_{\text{lift}} \cdot \dot{\mathbf{q}}_0 \\
0 &= \dot{\mathbf{q}}_0 - \dot{\mathbf{q}}_N + v_{\text{lift}} \cdot \mathbf{q}_0.
\end{aligned}
\tag{3.30}
$$

The mathematical background of Eqs. (3.29) and (3.30) is discussed in [44]. The Eqs. (3.26) - (3.30) are all boundary conditions and part of the periodicity constraint.

The resulting NLP is then formulated as

$$
\begin{aligned}
\min_{\mathbf{x}, z, \mathbf{u}, T} \quad & -\frac{1}{T} E(T) + \sum_{i=0}^{N-1} \mathbf{u}_i \mathbf{\Sigma}_{\mathbf{u}}^{-1} \mathbf{u}_i + K \\
\text{s.t.} \quad & \mathbf{F}(\dot{\mathbf{x}}_i, \mathbf{x}_i, z_i, \mathbf{u}_i, \mathbf{p}, T) = 0, && i = 0, \ldots, N-1 \\
& (3.25) - (3.30) && i = 0, \ldots, N-1 \\
& \mathbf{h}(\mathbf{x}_i, z_i, \mathbf{u}_i, \mathbf{p}, T) \leq 0, && i = 0, \ldots, N-1 \\
& \mathbf{G}(\mathbf{x}_i, z_i, \mathbf{u}_i, \boldsymbol{\theta}, T) = 0, && i = 0, \ldots, N-1 \\
& \mathbf{x}_{\min} \leq \mathbf{x}_i \leq \mathbf{x}_{\max}, && i = 0, \ldots, N-1 \\
& \mathbf{u}_{\min} \leq \mathbf{u}_i \leq \mathbf{u}_{\max}, && i = 0, \ldots, N-1 \\
& z_i \geq 0, && i = 0, \ldots, N-1 \\
& T_{\min} \leq T \leq T_{\max}, \\
& \mathbf{c}(\mathbf{x}_0, \mathbf{x}_N) = 0.
\end{aligned}
\tag{3.31}
$$

Together, the system dynamics $\mathbf{F}(\cdot)$ and the collocation equations $\mathbf{G}(\cdot)$ form the equality constraints $\mathbf{g}(\cdot)$ of Eq. (2.19). The path constraints $\mathbf{h}(\cdot)$ limit the system's power, energy, and velocity as well as angle of attack and the side-slip angle of the wing. The tether force is ensured to be non-negative. States, controls, and the final time T are bounded. The cost function mainly contains the maximization of the average power of one trajectory. The second term regularizes the control inputs with the positive definite term $\mathbf{\Sigma}_{\mathbf{u}}$ to penalize the high bandwidth of the control surfaces, avoiding overly aggressive manoeuvres. The term K defines a part of the cost function that varies depending on the specific problem that is to be solved. Certain parts are always involved in the term K as the penalization of the lift variable v_{lift} of Eq. (3.30).

3.4.2 Initial guess using a homotopy strategy

Due to the nonlinear system dynamics of Eq. (3.31), the NLP is non-convex and the NLP solver will only find local minima. In order to direct the solver

to a reasonable local minimum, a feasible initial guess is required. Without a good initial guess, the solver fails to converge and is not able to find any feasible trajectory. In order to find a feasible initial guess, a homotopy strategy is used as presented in [45] and briefly introduced in Section 2.2.4. The idea is to start with a less complex and less nonlinear problem and gradually retrieve the original problem formulation. The whole procedure is done with three steps:

1. Introduce artificial aerodynamic forces $\tilde{\mathbf{f}}_A$ and moments $\tilde{\mathbf{m}}_A$ and solve a trajectory-following NLP with a bounded final time $T_{\text{init}} \leq T \leq T_{\text{init}}$. Gradually retrieve the original aerodynamic forces $\mathbf{f}_A$ and moments $\mathbf{m}_A$ by modifying a homotopy parameter and solve the respective problems.

2. With the original aerodynamic forces and moments recovered, keep T fixed and solve the problem while gradually modifying the cost function from trajectory-following to power-maximizing.

3. As a last step, relax the tight bounds on the orbit time T, such that the orbit time can be optimized.

Mathematically, the homotopy-relevant part of the NLP can be described with two homotopy variables for the two homotopy procedures one and two as follows:

$$
\begin{aligned}
\min \quad & -\xi E(T) + (1-\xi)(\mathbf{x} - \hat{\mathbf{x}})^\top \mathbf{W}(\mathbf{x} - \hat{\mathbf{x}}) + K \\
s.t. \quad & \ddot{\mathbf{q}} = m^{-1}\left[\gamma\,\mathbf{f}_A + (\gamma-1)\tilde{\mathbf{f}}_A + \mathbf{f}_g + \mathbf{f}_{\text{Tdrag}} + \mathbf{f}_t\right], \\
& \dot{\boldsymbol{\omega}} = \mathbf{J}^{-1}\left[\gamma\,\mathbf{m}_A + (\gamma-1)\tilde{\mathbf{m}}_A - (\boldsymbol{\omega} \times \mathbf{J} \cdot \boldsymbol{\omega})\right], \quad \ldots,
\end{aligned}
\tag{3.32}
$$

with the homotopy parameters ξ in orange and γ in blue for enhanced visibility. In the first step, $\gamma = \xi = 0$ to obtain a trajectory-following problem with artificial forces and moments $\tilde{\mathbf{f}}_A, \tilde{\mathbf{m}}_A$. The artificial forces and moments are control inputs, allowing the optimizer to set their values directly. Initially, by enforcing $\gamma = 0$, the complex dynamics stemming from the aerodynamic forces and moments are completely disconnected. The values $\hat{\mathbf{x}}$ denote the predefined state trajectory with $\mathbf{W}$ as the weighting matrix for the trajectory-following problem. When this simpler problem has converged, the artificial quantities are gradually replaced with the actual aerodynamics $\mathbf{f}_A, \mathbf{m}_A$ by stepwise modifying $\gamma \to 1$. The step length is set to 0.1. With $\gamma = 1$, the full aerodynamics are recovered and the artificial controls no longer have any impact on the problem.

In the second homotopy, the actual power maximization problem will be recovered. While keeping $\gamma = 1$, the homotopy parameter ξ is increased

from zero to one by steps of 0.1 after each successful convergence. At $\xi = 1$, the original cost function is reached, optimizing the problem for maximal average power without any trajectory-following penalization.

At this point the orbit time is still fixed. Thus, in the final solution, the bounds on time T are relaxed to optimize flight velocity.

In the pumping-mode case, at this last instance the reel-out-orbit number is also set to a certain value. The final solution presents a local optimum. Fig. 3.6 shows an illustrative optimal trajectory for a pumping-mode system.
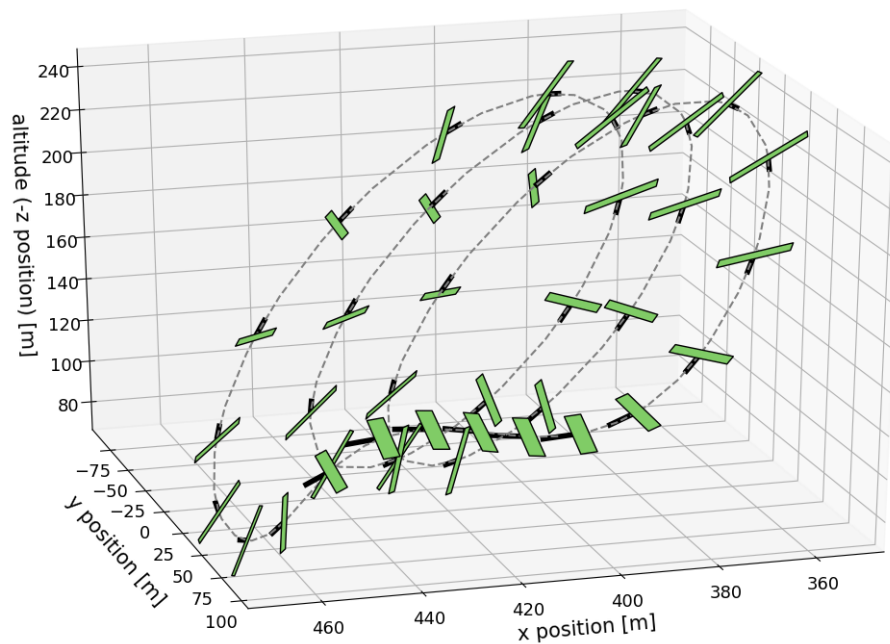
Figure 3.6: Optimal trajectory for the theoretical case of a pumping-mode system with a maximal tether length of $500\,\mathrm{m}$ and three reel-out orbits.

The entire homotopy procedure assists in gradually obtaining a feasible initial guess for the power optimization problem. The very first guess for the trajectory-following problem is given by describing a circular trajectory with an elevation angle of $30°$. The wing position, velocity, and angular velocity at the discretization points are chosen accordingly. The rotation matrix is initiated with the body-frame vectors $\mathbf{b}_x = \frac{\dot{\mathbf{q}}}{|\dot{\mathbf{q}}|}$, $\mathbf{b}_z = -\frac{\mathbf{q}}{|\mathbf{q}|}$, and $\mathbf{b}_y = \mathbf{b}_z \times \mathbf{b}_x$, with $\mathbf{R} = [\mathbf{b}_x, \mathbf{b}_y, \mathbf{b}_z]$. When modelling the pumping-mode system, the NLP is initialized with a single pumping orbit. The number of orbits is then changed in the end as a final operation after the two homotopy procedures, as described above.

3.5 Large-scale wind data

The NLP (3.31) computes the power generation of a single system for a specific wind condition, so far assumed to be a simple logarithmic profile. In this thesis, the AWES model is used for a variety of studies ranging from wind-farm control to power-system optimizations, using time- and location-dependent wind data. This section presents the wind data and the implementation in the OCP and describes the method of handling a large set of wind data in the OCP for computing annual power-generation profiles.

3.5.1 Wind data

At the beginning of this chapter, in Section 3.1.2, we mentioned two possible methods of modelling the wind profile: the standard wind profile computed with the power law (Eq. (3.8)) and a profile computed using wind data from reanalysis models in the form of polynomials. In Papers B and D, the wind data are taken from the "Modern-Era Retrospective analysis for Research and Applications version 2" (MERRA-2) [36], an atmospheric reanalysis provided by NASA. In order to cover a wide altitude range, a wind-data set for low- [46] and a data set for high- [47] altitude wind speeds need to be combined. The resulting data set has a vertical range up to 800 m, given by 10 data points (more dense at the lower altitudes). The data set shows a $0.625° \times 0.5°$ longitude-by-latitude spatial resolution and the temporal resolution is three-hourly. Paper E uses the more recently updated ERA-5 wind data, which have a spatial resolution of $0.25° \times 0.25°$ and a temporal resolution of one hour. Here the vertical wind speeds are given in sigma levels, providing 15 data points up to the altitude of 800 m. Even though wind speeds are available at higher altitudes, 800 m is chosen as the upper level because the maximal operational altitude is constrained by the tether length, which we have set to 500 m, in accordance with the Makani prototypes [40].

The instantaneous wind data at each altitude point are given in the common meteorological vector conventions: a North/South and a West/East vector. The system model is independent of the compass direction, and instead the wind vector is aligned with the x-axis of the Earth reference frame (see Fig. 3.1). For this transformation, the main wind direction of all instantaneous vertical wind data points are projected to one main direction and an orthogonal deviation, i.e. an x and y component. Fig. 3.7 illustrates the transformation of raw wind data to the wind profile function implemented in the model. On the left, Fig. 3.7 illustrates original wind vectors in their compass direction. On the right, wind vectors are illustrated in the Cartesian coordinate frame as implemented in the model. The vectors $\boldsymbol{w}_{\mathrm{v,x}}$ and
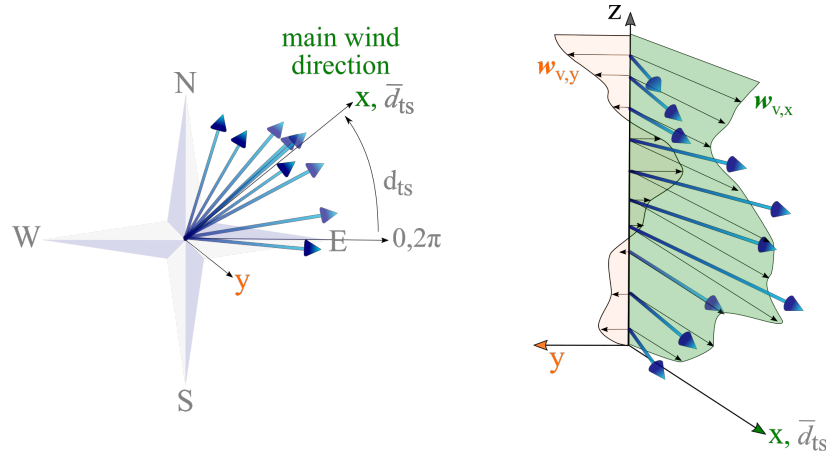
43

Figure 3.7: Illustration of wind-data processing. Wind data are given as vectors in the compass direction for each of the, here, ten altitude levels. The main wind direction and angular deviation are illustrated in the Euclidean plane (left). In the model, the main wind direction $\bar{d}_{ts}$ (here, illustratively northeast) is aligned with the x-axis of the Earth frame. The wind speeds are then expressed as main wind components and their orthogonal deviations in the matrix of vertical wind parameters $\boldsymbol{w}_v \in \mathbb{R}^{n_{lev} \times 2}$ (right).

$\boldsymbol{w}_{v,y} \in \mathbb{R}^{n_{lev}}$ are the wind data that belong to one vertical profile and are collected in $\boldsymbol{w}_v \in \mathbb{R}^{n_{lev} \times 2}$ with n_{lev} as the number of vertical data points. In order to obtain a wind profile as a smooth function of the altitude, the data are interpolated. As interpolation method a Lagrange polynomial is chosen. The theory of the Lagrange polynomial is detailed in Section 3.2.2, and the polynomial is defined in Eq. (2.5). The choice of a Lagrange polynomial for the interpolation is motivated by the fixed number of polynomial parameters $\boldsymbol{\theta}$. By using a Lagrange polynomial, the wind data $\boldsymbol{w}_{v,x}$, $\boldsymbol{w}_{v,y}$ determine the polynomial parameters $\boldsymbol{\theta}$, which implies that the number of these parameters ($= n_{lev}$) can be kept the same during the modelling for all wind profiles without loss of accuracy. In this case, the parameters are chosen so that they are close to the actual wind speeds $\boldsymbol{w}_v$ at their respective altitudes $\mathbf{a}$, but also so that the second derivative of the polynomials is penalized with a weighting factor k. To obtain these parameters we solve the minimization

$$\boldsymbol{\theta}_x = \arg\min_{\boldsymbol{\theta}_x} \quad \frac{1}{2}\|p_{\mathcal{L}}(\mathbf{a}, \boldsymbol{\theta}_x) - \boldsymbol{w}_{v,x}\|^2 + k \cdot \left\|\frac{\partial^2 p_{\mathcal{L}}(\mathbf{a}, \boldsymbol{\theta}_x)}{\partial \mathbf{a}^2}\right\|^2 \tag{3.33a}$$

$$\boldsymbol{\theta}_y = \arg\min_{\boldsymbol{\theta}_y} \quad \frac{1}{2}\|p_{\mathcal{L}}(\mathbf{a}, \boldsymbol{\theta}_y) - \boldsymbol{w}_{v,y}\|^2 + k \cdot \left\|\frac{\partial^2 p_{\mathcal{L}}(\mathbf{a}, \boldsymbol{\theta}_y)}{\partial \mathbf{a}^2}\right\|^2, \tag{3.33b}$$

where $p_{\mathcal{L}}$ denotes the Lagrange polynomial, which is a function of the al-

titude $\mathbf{a} \in \mathbb{R}^{n_{lev}}$, the positive altitudes of the respective wind data points (in the model the altitude is $-z$). The parameter vectors $\boldsymbol{\theta}_x$ and $\boldsymbol{\theta}_y$ denote the polynomial weighting parameters for the respective polynomial wind profiles in the x and y-direction. The parameters $\boldsymbol{\theta} = \{\boldsymbol{\theta}_x, \boldsymbol{\theta}_y\}$ are then implemented as part of the general parameters $\mathbf{p}$ in the AWES model (3.15). The penalization parameter for the polynomial's second derivative is set to $k = 10^4$. Fig. 3.8 shows polynomial wind-speed profiles for the x-axis component of the wind reference frame. On the left the figure shows a range of profiles from low to high wind speeds; on the right four profiles including the original wind data points $\{\boldsymbol{w}_x, \mathbf{a}\}$ are illustrated to show the effect of the minimization problem (3.33).
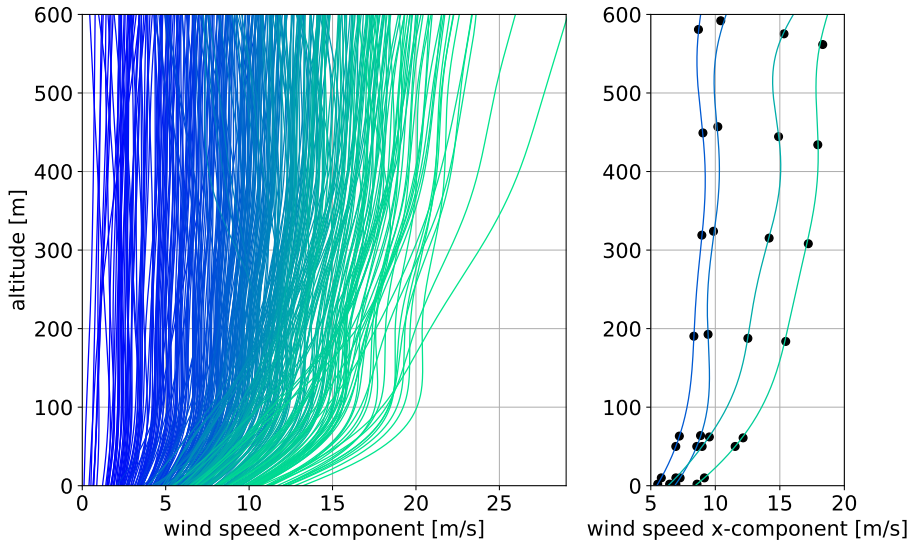
Figure 3.8: Polynomial wind profiles for the x-axis component of the wind model. The figure's y-axis denotes the altitude and the x-axis the wind speeds. Left: Range of low wind-speed (blue) to high wind-speed profiles (green). Right: Illustration of original wind data $\{\boldsymbol{w}_x, \mathbf{a}\}$ and corresponding polynomial, obtained with (3.33).

3.5.2 Solving OCPs for large wind data

The wind profiles are implemented into the NLP with the aim of computing annual generation profiles of the AWE system at specific locations. The work that uses the power-generation profiles is presented in Chapter 4.

In order to compute an hourly generation profile for a large set of locations and time points, the NLP (3.31) has to be solved repeatedly for each vertical wind profile, expressed by the data points $\{\boldsymbol{w}_v, \mathbf{a}\}$ (or in fact $\{\boldsymbol{\theta}, \mathbf{a}\}$). Given

the complex solving procedure including the tedious initial guess-finding method (Section 3.4.2, a less time-consuming method is preferred to solve the numerous NLPs. The reason for not simplifying the model at this point and continuing using an optimal control approach is the otherwise resulting loss of information related to operational altitudes, flight orbit, and other state trajectories.

Homotopy-path-following
This thesis proposes a method that reduces the computation time for solving a large family of NLPs with different wind parameters. The method is thoroughly explained in Paper B. The method is based on the homotopy strategy presented in Section 2.2.4. The main idea is to sort the available wind data in such a way, that when solving the related NLPs consecutively, the NLP solutions are in the neighbourhood of the optimal solution of the previous solved NLP. We sort the wind parameters by the wind speed at the average operational height of the AWES, which has been found sufficient as the optimal operational height turned out to be mainly around the average operational height. The sorting of wind parameters thus allows for taking the solution of an NLP as the initial guess for the NLP next in line to be solved. We refer to this method as the *homotopy-path-following* method but this approach for parametric NLPs is also known as the continuation method [48].
The individual NLPs are all solved with the Primal-Dual Interior Point (PDIP) method using the solver IPOPT. To enable the initialization of the problems with a prior optimal solution requires a constant barrier parameter τ for the PDIP. Here, we choose $\tau = 10^{-4}$. Applying the wind-parameter sorting and the fixed-barrier parameter reduces the computation of one wind profile 20-fold. The reduction of the solution accuracy due to fixing the barrier parameter is found to be negligible.

Regression model
For studies that require an annual generation profile for several hundreds of locations, the homotopy-path-following method can still be quite tedious. Also, at this scale, the detailed state trajectories for each NLP solution might be of less importance. Thus, a regression model in the form of a random forest regression is trained to map the wind data to the respective power output. Approximating the power output with this method decreases the computation time drastically compared to the homotopy-path-following strategy. The mean absolute error of the random forest model with respect to the NLP results in $\varepsilon = 4 \cdot 10^{-3}\,\mathrm{MW}$. This is assumed to be acceptable in large-scale studies, where power outputs are averaged over regions.

4

Large-scale deployment of AWE

The power-generation potential of the AWE technology is expected to be high, offering global motivation for companies and academia to pursue development and commercialization. As of today, AWE technology is still in its early phase (TRL[1] 4-5) [15], but the technology has been suggested for both niche applications in remote off-grid areas and large-scale grid deployment. Use in off-grid areas would entail smaller systems that may even be mobile, like Enerkite's container concept [4]. In the case of large-scale deployment, large quantities of AWE systems are considered for onshore as well as deep offshore locations. The latter presents an expected advantage for an AWES relative to a traditional WT as no ground-fixed foundation is needed for AWESs [1, 11]. As an example, the former company Makani Power had its first prototype tested offshore in Norway in 2019 [49].

Moving towards large-scale deployment requires stakeholders and investors that have a clear understanding of the system's electric power performance, system costs, and its interplay with other technologies in order to avoid risky investments. However, there is still a lack of analyses, reports, and investigations in this field of research [15]. This thesis investigates the potential role of the AWE technology in a future, decarbonized power system and identifies challenges and possibilities for large-scale deployment of AWE from a technical and economic perspective.

The technical challenge investigated in this thesis relates to the periodically fluctuating power generation of an AWES within a short time scale of less than a minute. In a wind farm, this issue bears the risk of large superimposed

---

[1]Technology Readiness Level

fluctuations in the total farm power output. This risk can be eliminated, for example by batteries or controlling the individual systems into a shifted synchronous flight pattern. The latter approach is discussed in Section 4.1 and in more detail in Paper C.

The economic challenge investigated in this thesis relates to the power-generation profile over a longer time scale of hours to months. In order to deploy AWESs in an electricity generation system on a large scale, the value of the electricity generated must exceed its cost. The costs of AWESs are difficult to determine, as the technology is still in an early phase of commercialization. The value of the electricity generation can, however, be assessed, providing an upper limit for the cost of an AWES for large-scale deployment. This assessment is presented in Section 4.2 and in more detail in the Papers D and E.

4.1 Technical integration challenges - variability on a sub-minute scale

Large-scale deployment of AWE in the power system implies the installation of multiple systems in the form of wind farms. Wind farms, such as all large-scale grid-connected capacity, are expected to deliver high power quality, i.e. a smooth power output. A single AWES shows periodic power fluctuations with a frequency of per sub-minute scale. The fluctuations are caused by gravity and the normal wind shear[2], forcing the power-generating wing into an asymmetric flight pattern. In the case of the pumping-mode technology, the periodic fluctuations are especially large. Its power generation is cyclically interrupted due to the retraction of the wing, which even consumes a fraction of electric power. The power-generation profiles of a drag-mode and of a pumping-mode system are visualized for a few flight orbits in Fig. 4.1. One orbit is considered one period.

Modern power systems are used to deal with the fluctuations arising from well-established sources of renewable energy. However, the severe periodic fluctuating power profiles of AWESs, especially in pumping-mode, are rather unusual compared to other technologies, and the potential impact on the power grid is unclear. Future AWE farms may be expected to be required to deliver a smooth power output.

There are three main options for dealing with the periodic power fluctuations of the AWE systems: on-site chemical storage (batteries), on-site kinetic storage (flywheels), or internal smoothing through wind farm control.

---

[2]The wind shear denotes the changing wind speeds with altitude.

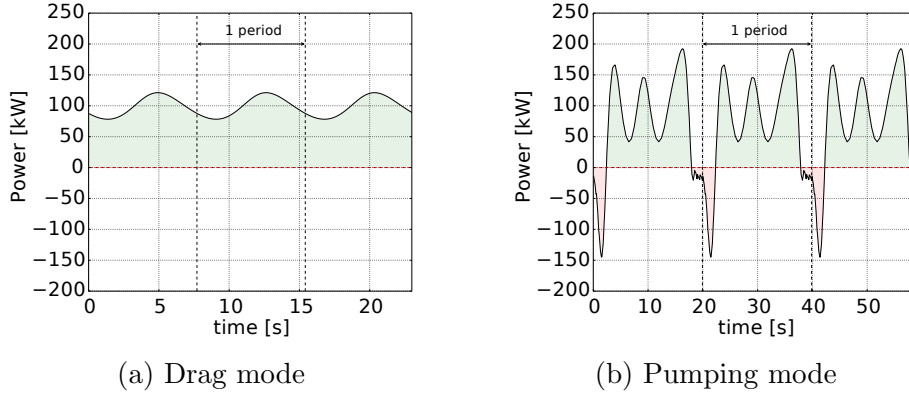(a) Drag mode   (b) Pumping mode

Figure 4.1: Characteristic power production profile for a short time period obtained by the drag-mode and pumping-mode systems. One can observe the power consumption of the pumping-mode system each orbit. Here, the average power output results in 48.4 kW and 56.74 kW, respectively.

This thesis looks into the latter, the tentative solution of balancing the power fluctuations within an AWE farm by controlling the flight trajectories of the AWESs. For an AWE farm with pumping-mode systems, this means shifting the periodical retraction phase of the wing so that the power required for the retraction is provided by the neighbouring AWE systems in the same farm. For an AWE farm with drag-mode systems, the phase-shifted trajectories would dampen the fluctuations induced by gravity, leading to smoother power generation across the farm. Hence, the individual systems within a farm are all controlled to fly their cyclical trajectory at a constant speed in order to stay phase-shifted relative to each other. The downside of this control strategy is the power loss due to restricting the AWESs to a sub-optimal flight velocity. For an optimal velocity, each individual system in a farm would adjust its flight trajectory and speed to the local wind condition to pursue maximal power output. We quantify this lost power generation.

Instead of modelling a complete wind farm, we consider a single AWES. It is assumed that wake effects can be neglected as they only play a minor role in AWE farms [50]. The optimal average power generation at prevailing wind conditions is computed with the OCP, which is formulated in Section 3.4. A sensitivity analysis is performed with respect to the prevailing wind speed, first enforcing a *fixed* orbit time and then with a *free* orbit time. A fixed orbit time means optimizing the flight velocity with respect to the *mean* wind speed $\bar{w}$ of the overall wind farm, which leads to a constant flight velocity for all individual AWESs. A free orbit time implies optimizing the flight velocity to local wind speeds $\bar{w} + \Delta w$, such that the optimal flight

49

velocities of the individual AWE systems differ. The latter operation leads to a maximal average power generation for the wind farm, but also to possible high variations in the total farm power output as periodic fluctuations could get superimposed. As these variations should be avoided, a controlled equal flight velocity of all individual systems is preferred in reality, even if it implies a sacrifice in total power generation. We find that the relative percentage power lost by not individually optimizing the flight velocity does not exceed 4%. This study quantifies the power loss when choosing the farm control for mitigating the fluctuations. For investigating further the economical cost of this option, the value of the lost electricity needs to be analysed and compared to the other mitigation options, mentioned above.

In the following we assume that the operation of the individual systems within a wind farm are optimized for local wind conditions in order to account for the maximum possible power generation. Also, it is assumed that a farm of AWESs can be operated so that the power output is smooth and any high-frequency power issues are resolved at low cost and do not impact operational and investment costs.

4.2 Economic integration challenges - variability on the hourly scale

Beyond the power production variations at sub-minute scale, the variations at an hourly, weekly, and monthly scale are also of importance. Previous work on the wind resource and the theoretical generation of AWESs indicates that AWESs are expected to have a higher power yield, provide a more constant generation, and be less costly than traditional WTs due to the ability of tapping into high-altitude wind fields [18, 20, 51]. However, more detailed investigations on detailed power-generation profile analyses and comparisons with other power-generation technologies are necessary to evaluate the conditions for large-scale AWE deployment [15]. Due to the expected large installations of WTs in Europe [52], which exploit the same varying resources for electricity generation as AWE, a comparison between AWE generation patterns and traditional wind-power generation is of particular relevance. The economic viability of the AWE technology depends on the cost per unit of installed capacity relative to the amount of electricity produced per unit of installed capacity and on the *value* of this produced electricity, which is determined by the temporal distribution of the electricity production over a year. This temporal distribution is of particular relevance in future electricity systems in which large shares of variable renewable energy technologies such as wind power plants and pho-

tovoltaic systems are expected. The greater the share of renewable energy, the greater the variability in total power generation, which has to be balanced in order to meet the demand at all times. The most ideal and valuable power-generation profile of AWESs would follow the load. However, since there is no correlation between the variability of electricity demand and that of wind-power generation [53], the lower the temporal variability of power generation for AWESs, the higher the *value* of the generated electricity. In the following, the value of how the temporal distribution of the annual electricity generation benefits the power system is referred to as the *profile value*.

The traditional wind-power technology is by today a well-established, low-cost electricity source, which makes it interesting to compare the power generation of traditional WTs and AWESs. Ideally, these would differ in such a way that periods of high generation for the one technology compensate periods of low generation for the other. However, even though they operate at different altitudes, AWESs and traditional wind turbines harvest the same resource of variable wind energy and are therefore likely to show correlated power-generation profiles.

To analyse this, generation profiles for both technologies are computed for a large number of grid points using the real wind data from ERA5 and MERRA resources, presented in Section 3.5.1. The AWES generation profiles are computed for all available wind data by means of the homotopy-path-following method and the regression model presented in Section 3.5.2 and in greater detail in Paper B. The power-generation profiles for the WT are computed using a general machine power curve of a Vestas WT [54] detailed in Papers D and E.

We investigate the degree of similarity between the power generation of an AWES and that of traditional wind turbines, and how the former is valued in the electricity generation system, using several methods and quantification tools, which are presented next. The more detailed analyses can be found in Papers D and E.

4.2.1 Performance indicators

This section summarizes the performance indicators used to quantify and investigate the power-generation profiles of the modelled AWESs and WTs.

Power profile quality
The economic value of AWE depends largely on the *generation profile*, which presents the hourly averaged distribution of the electricity generation over a year. In the initial analysis, the generation profile of an AWES is compared

directly to that of a WT and different aspects are investigated.

First, the *variability of the electricity generation* over a year is determined using the Gini coefficient [55]. The Gini coefficient was originally developed to quantify social inequality; here, it serves as a measurement of variability of electricity generation distributed during a year. The Gini coefficient is determined by sorting and adding the available data of hourly generation in an ascending order, as in a cumulative profile. This gives a quantification on how similar the individual data points are. In this study case, if at each point in time the same amount of electricity is produced, the Gini coefficient equals 1, implying complete uniformity. If the production is concentrated to a few hours of the year, the Gini coefficient becomes low, indicating highly variable power generation.

Second, the *Load Duration Curve (LDC)* is determined by sorting the chronological generation profile by power level, starting with the highest power production. From the LDC one can directly identify the *Full Load Hours* (FLHs)[3], the number of low production hours, and the downtime[4] of the technology.

Third, the *correlation* between the generation profiles of the WT and the AWES is measured using the squared Pearson correlation coefficient R^2. The coefficient ranges between 0 and 1 and represents the square of the linear correlation between two data sets, i.e. here, the correlation between the generation profile of the AWES and the WT. A coefficient close to 1 indicates a high correlation, implying similar temporal variations in the generation pattern, while a low coefficient indicates a low correlation.

Using these three performance indicators on the generation profiles for an AWES and for a WT provides a wide-ranging assessment, which can be used to present differences between the two wind-power technologies.

There are additional technologies that need to be considered in an electric power system, and the resulting system dynamics influence the relation between the AWES and WT power generation. In order to study the interactions, AWESs are implemented in a regional investment model of the electricity system in order to consider the technology and its generation profiles in a larger system perspective. Here, instead of comparing the generation profiles of single systems, wind farms are considered. Thus, for computing the generation profiles of the WT and the AWES farms that are implemented in the model of the electricity system, the wind-speed data

---

[3]Full Load Hours: Number of hours it would have taken to produce the annual generated energy if operating constantly at rated capacity.

[4]Downtime: Hours of zero production

are assumed to be normally distributed with a standard deviation of $\sigma = 1\text{m/s}$. This smooths the power generation of the technologies, as is the case for wind farms.

Marginal System Value (MSV)

The electricity-system model used in this thesis was originally developed to investigate the combinations of technologies for power generation that can meet the electricity demand at the lowest annual system cost. For these investigations, investment and operational costs for the different technologies are key parameters in the model. As the AWES costs are very uncertain, the AWES investment cost cannot be implemented directly in the model. Instead, an alternative approach, namely investigating the *Marginal System Value* (MSV) of AWESs to the electricity system is pursued. The MSV is the economic value of increasing the AWE capacity in the electricity system. The MSV can also be related to the "willingness to pay" for an additional investment in AWESs.

The MSV is obtained from the electricity-system model by enforcing a fraction of the total regional demand to be supplied by AWE. As the MSV differs depending on the initial AWE share, the share is increased stepwise from 0 to 1 by steps of 0.1 between individual model runs. In the model, the AWE technology is not linked to any costs, so that it provides a theoretical free energy source. Increasing the AWE share of the electricity supply thus entails a reduction in the investment and variable costs of the electricity system. This reduction in system costs corresponds to the value of the additional installed capacity of AWE. As a result, the MSV of AWE represents an upper bound for AWE costs if the AWE is to supply a certain share of the electricity demand.

In general, the *annual* marginal system value $c'(\xi)$ is mathematically defined by the partial derivatives of the total system cost $c_{\text{tot}}(\xi)$ and the installed capacity of AWE $s(\xi)$ at an energy share of ξ as

$$c'(\xi) = \frac{\partial\, c_{\text{tot}}(\xi)}{\partial\, s(\xi)}. \tag{4.1}$$

For the sake of simplicity, the derivatives are evaluated via finite differences, according to

$$c'(\xi) = \frac{\Delta c_{\text{tot}}(\xi)}{\Delta s(\xi)} = \left| \frac{c_{\text{tot}}(\xi + 0.05) - c_{\text{tot}}(\xi - 0.05)}{s(\xi + 0.05) - s(\xi - 0.05)} \right| \quad \xi = 0, 0.1, ..., 1, \tag{4.2}$$

where $\Delta c_{\text{tot}}(\xi)$ is the change in total electricity system cost and $\Delta s(\xi)$ the change in installed AWE capacity at an AWE share ξ of the regional annual

electricity demand. Dividing the annual marginal system costs (4.2) by the annuity factor AF^5 leads to the marginal system value $MSV(\xi)$ defined as

$$MSV(\xi) = c'(\xi) \cdot \frac{1}{AF} \quad \text{with} \quad AF = r^{-1} \left(1 - \frac{1}{(1+r)^t} \right), \qquad (4.3)$$

where $r = 0.05$ is the interest rate and $t = 30$ the assumed AWE lifetime. The MSV, defined as (4.3) could be compared to the maximal present value (capital costs including projected O&M[6] costs) of an AWES per MW that is economical in a cost-optimized electricity system. The electricity-system model is detailed in the next section and in the appendix of Paper E.

4.2.2 Mathematical model of the electricity generation system

The electricity-system model used for this study is formulated as a Linear Programming (LP) problem with the objective of minimizing total annual system costs for investment and dispatch of power plants to meet the demand for electricity in a specific region. The optimization is subjected to the generation-load balance as well as constraints related to technology, resource, and emission limitations.

The model is set up as a *green-field study*, i.e. assuming no prior installation of power plants. The purpose of the model is to study the generation and load dynamics of a regional system with net-zero CO_2 emissions. The main decision variables of the LP problem are the installed capacity of each technology and their hourly power generation.

The regions in this study are chosen to be Ireland (IE), Hungary (HU), central Spain (ES3), and south-central Sweden (SE2), which differ in the availability of renewable energy resources, e.g. wind and solar insolation. All regions are modelled in isolation, neglecting any inter-regional trade. Grid limitations and losses are disregarded and perfect foresight is assumed. More information on the numerical data, e.g. technology costs, can be found in Paper E.

The power-generation profiles for the modelled AWESs and the WT are computed for each available latitude-longitude grid point ($0.25° \times 0.25°$ resolution) in the mentioned regions, using ERA5 wind data and previously described methods. In this analysis, the generation profiles are computed assuming farms rather than single systems. Hence, the wind-speed data are assumed to be normally distributed with a standard deviation of $\sigma = 1\mathrm{m/s}$. This smooths the power generation curves of the technologies. Using these

---

[5]Annuity factor transforms an annual payment into a present value
[6]Operation and Maintenance

large wind-data sets results in a large amount of profiles to be implemented in the electricity-system model, so the data are reduced by aggregating the profiles into five different wind classes per region. The profiles are classified via percentiles of the wind speed at 100 m. Each wind class holds a respective averaged representative power-generation profile and the related area, where this profile is available. This aggregation reduces the size of the LP problem as the model now has a choice between only five different AWE and WT generation profiles per modelled region, instead of several hundred.
The different AWESs modelled are implemented in individual model runs to separate the system dynamics to obtain a clear interpretation and because it is assumed that the technology development will converge to the AWE configuration that is most relevant in the future electricity generation system. Hence, in the following technology descriptions, the subscript "AWE" stands for the respective modelled system.
All technologies included in the model results are listed in Table 4.1. The

Table 4.1: Technologies included in the model results

· Airborne wind energy system of wind class 1,2,3,4,5 [1]
· Onshore wind turbine of wind class 1,2,3,4,5
· Hydro power with storage
· Nuclear power
· Photovoltaic with fixed optimal tilt (crystalline silicon cells)
· Biogas-fuelled combined cycle gas turbine
· Biogas-fuelled open cycle gas turbine
· Combined cycle gas turbines with CCS, fuelled by 90% natural gas and 10% biogas

[1] The area defined by a certain wind class for WTs is the same as that defined for that wind class for the AWESs.

model is presented immediately below. The sets (uppercase letters in curly font), parameters (uppercase letters), and variables (lowercase letters) are listed in the following Table 4.2. Variable and parameter notations are in no correlation to definitions in previous chapters.

Table 4.2: Sets and variables of the LP problem. Decision variables are denoted with lowercase letters while given parameters are presented with uppercase letters.

Set		Description
$\mathcal{I}$		Set of technologies
$\mathcal{I}_{\mathrm{th}}$		Subset including all thermal technologies
$\mathcal{T}$		Set of time steps
$\mathcal{J}$		Set of time steps comprised in a start-up interval
Variable	**Unit**	
$g_{i,t}$	GW	Generation of technology i at time step t
s_i	GW	Installed capacity of technology i
$g_{i,t}^{\mathrm{active}}$	GW	Active capacity of a technology i at a time t
$c_{i,t}^{\mathrm{cycl}}$	k€	Cycling cost
$c_{i,t}^{\mathrm{start}}$	k€	Start-up cost
$c_{i,t}^{\mathrm{part-load}}$	k€	Part-load cost
$soc_{\mathrm{hydro},t}$	GWh	Hydro power storage at time t
Parameter	**Unit**	**Description**
D_t	GWh	Electricity demand of a region at time step t
L_i^{min}		Minimum relative load level for a technology i
ρ_{P}	GW/km²	Power density for either AWE or WT
A_k	km²	Area available for wind instalment in class k
$G_{i,t}$	-	Weather-dependent profile for technology i at time t
C_i^{inv}	k€/GW	Investment cost of technology i
C_i^{run}	k€/GW	Operational cost of technology i
C_i^{start}	k€/GW	Starting cost per GW
$C_i^{\mathrm{part-load}}$	k€/GW	Part-load cost per GW
AF_i		Annuity factor for technology i
q_t^{in}	GWh	Water inflow for hydro power

Objective cost function for the LP problem

The cost function of the LP problem minimizes the total system costs as

$$c^{\mathrm{tot}} = \sum_{i\in\mathcal{I}} AF_i\, C_i^{\mathrm{inv}} s_i + \sum_{i\in\mathcal{I}} \sum_{t\in\mathcal{T}} (C_{i,t}^{\mathrm{run}} g_{i,t} + c_{i,t}^{\mathrm{cycl}}), \qquad (4.4)$$

where the decision variable c_{tot} is the total annual system cost and $g_{i,t}$ the generation capacity of technology i at time t. The parameter $C_{i,t}^{\mathrm{run}}$ denotes the operational, or running, costs, including variable O&M and fuel costs per GW for a technology i. The variable $c_{i,t}^{\mathrm{cycl}}$ is the thermal cycling cost and C_i^{inv} the initial investment cost per GW of a technology i. The annuity factor AF_i is dependent on the technical lifetime of a technology i at an interest rate of 5%.

Demand - supply balance equations

At each time step t the electricity demand has to be met by the generation as

$$\sum_{i \in \mathcal{I}} g_{i,t} \geq D_t \qquad \forall t \in \mathcal{T}, \tag{4.5}$$

where $\mathcal{I}$ is the set of all technologies and $\mathcal{T}$ the set of time steps (every third hour of the year). The parameter D_t denotes the demand profile of the respective region and $g_{i,t}$ the generation of technology i at time step t. The generation $g_{i,t}$ is limited by the installed capacity s_i and weighted by a parameter $G_{i,t}$. The parameter $G_{i,t}$ is a weather dependent profile for solar and wind-power technologies, while for other technologies, $G_{i,t} = 1$ at all time steps $t \in \mathcal{T}$. The instantaneous power generation of a technology i is then defined as

$$g_{i,t} \leq G_{i,t} \cdot s_i \qquad \forall t \in \mathcal{T}, i \in \mathcal{I}. \tag{4.6}$$

The current storage of hydro power $soc_{\text{hydro},t}$ at time t is constrained by the water reservoir, by the maximum power plant capacity and the weather dependent inflow q_t^{in} as

$$soc_{\text{hydro},t} \leq s_{\text{hydro}} \qquad \forall t \in \mathcal{T} \tag{4.7}$$

$$soc_{\text{hydro},t+1} \leq soc_{\text{hydro},t} + q_t^{\text{in}} - g_{\text{hydro},t} \qquad \forall t \in \mathcal{T}. \tag{4.8}$$

Area availability for wind

It is assumed that AWESs and WTs compete for the same sites, thus a constraint is added such that only one technology can be installed per location. Each wind class consists of a maximum area that is linked through the following constraint:

$$\frac{s_{\text{WT}\{k\}}}{\rho_{\text{P,WT}}} + \frac{s_{\text{AWE}\{k\}}}{\rho_{\text{P,AWE}}} = A_k \qquad \forall k \in \{1, 2, 3, 4, 5\}, \tag{4.9}$$

where k is the wind class, $\rho_{P,\cdot}$ the power density [$^{\text{GW}}/_{\text{km}^2}$] of AWE and WT, respectively, and A_k the available area [km^2] in class k. The available area is restricted by cities, inland water, nature reserves, and the borders of the modelled region.

AWE production share

For the analysis in this work, the total AWE generation (including curtailment[7]) of all five classes (AWE1, ..., AWE5) is constrained to supply a certain share ξ of the total electricity demand, formulated as

$$\sum_{t \in \mathcal{T}} D_t \cdot \xi = \sum_{k=1}^{5} \sum_{t \in \mathcal{T}} s_{\text{AWE}\{k\}} \cdot G_{\text{AWE}\{k\},t}. \tag{4.10}$$

---

[7]Curtailment: Cutting power production to avoid excessive electricity generation

This constraint is needed for the estimation of the MSV.

Thermal cycling
Thermal electricity generation technologies are limited by their cycling properties (start-up and minimal load abilities). The generation of technology i is bounded by the minimum load and the hot capacity, which is defined as

$$g_{i,t} \leq g_{i,t}^{\text{active}} \qquad \forall t \in \mathcal{T}, i \in \mathcal{I}_{\text{th}}, \tag{4.11}$$

where $\mathcal{I}_{\text{th}}$ is the set of thermal power plants and g^{active} is the active capacity of a technology i at each time step t. If a plant i is active, the active generation needs to be larger than the minimum load level L_i^{min} as

$$L_i^{\text{min}} g_{i,t}^{\text{active}} \leq g_{i,t} \qquad \forall t \in \mathcal{T}, i \in \mathcal{I}_{\text{th}} \quad \text{and} \quad L_i^{\text{min}} = [0,1]. \tag{4.12}$$

The start-up capacity $g_{i,t}^{\text{start}}$ at time t of a technology i is constrained by the current active capacity as

$$g_{i,t}^{\text{start}} \geq g_{i,t}^{\text{active}} - g_{i,t-1}^{\text{active}} \qquad \forall t \in \mathcal{T}, i \in \mathcal{I}_{\text{th}} \tag{4.13}$$

and constrained by the minimum start-up time as

$$g_{i,t}^{\text{start}} \leq s_i - g_{i,t-j}^{\text{active}} \qquad \forall t \in \mathcal{T}, j \in \mathcal{J}, i \in \mathcal{I}_{\text{th}}, \tag{4.14}$$

where $\mathcal{J}$ is a set of time steps comprised in the start-up interval. The related cycling costs $c_{i,t}^{\text{cycl}}$ are then a combination of start-up and part-load costs and defined as

$$c_{i,t}^{\text{cycl}} \geq g_{i,t}^{\text{start}} C_i^{\text{start}} + (g_{i,t}^{\text{active}} - g_{i,t}) C_i^{\text{part-load}} \qquad \forall t, \in \mathcal{T}, i \in \mathcal{I}_{\text{th}}. \tag{4.15}$$

The whole electric power generation is constrained by the annual net emissions as

$$\sum_{t \in \mathcal{T}} \sum_{i \in \mathcal{I}_{\text{th}}} E_i \, g_{i,t} + E_i^{\text{start}} g_{i,t}^{\text{start}} + E_i^{\text{part}} (g_{i,t}^{\text{active}} - g_{i,t}) \leq E_{\text{cap}}, \tag{4.16}$$

where E_{cap} the total allowed emission in kg of the system in one year. In this thesis, $E_{\text{cap}} = 0$.

This model is used to evaluate the MSV of the different AWES designs introduced previously in Section 3.2.2. The AWESs are modelled with two different power-density factors ρ_P, in order to obtain a sensitivity that accounts for the uncertainty of farm power density and total area availability.

4.2.3 Results and discussion on the large-scale deployment

This section presents the results of the investigation regarding the large-scale potential of the two modelled drag-mode AWESs: A small 666 kW wing with a 26 m span and a larger 2 MW wing with a 40 m span. First, a short summary of the whole procedure is given. The two AWESs are introduced in Section 3.2, visualized in Fig. 3.3, and implemented using the numerical data listed in Table 3.3. A large number of annual generation profiles are computed using high-resolution temporal and spatial MERRA and ERA5 wind data (Section 3.5.1), and the power-maximizing OCP (Section 3.4). We investigate the generation profiles using the different performance indicators: the Gini coefficient, the LDC, and the correlation coefficient R^2, introduced in Section 4.2.1. The generation profiles, computed by assuming wind farm configurations, are further implemented in the electricity-system model to evaluate the MSV of AWE in the electricity system.

AWE annual power-generation profile
By comparing the power-generation profiles of AWESs to the profile of the modelled traditional WT at several different European locations, the following results can be highlighted:

- The generation profiles of the two technologies are highly correlated in all regions as the technologies generate power at similar times. This is indicated by a high correlation coefficient.

- A 2 MW AWE system obtained by aligning three of the small AWE wings (as Fig. 3.3c) results in the highest annual power generation by far, indicated by a high number of FLHs. This is due to the large area-to-weight ratio of the small wing, the low specific power[8], and the low tether drag. However, in terms of downtime, the WT performs better compared to any of the AWESs.

Comparing the normalized power profiles of the small to the large AWE wing shows that

- the smaller AWE wing with the smaller wing span and smaller generator has less downtime and a less variable power distribution during the year than the large AWES with its greater wing span and greater capacity.

We find that our results are determined by the following two factors: the wing design and the regional wind conditions.

---

[8]Specific power of AWES: generator capacity per wing area $^{MW}/_{m^2}$

First, the power performance of the wings largely depends on the wing parameters chosen in the model. At the time of this study, no commercial large-scale wing was available. Thus, wing parameters of the modelled AWE systems are taken partly from company information and partly from articles and books. Changing the design parameters could indeed lead to different results for the power generation. The decisive factors influencing the wing performance are the area-to-weight ratio and the rated capacity (generator size) of the wing, which are important design choices. The area-to-weight ratio is related to the positive relation of lift force and wing area. The rated capacity is related to the variability of power generation during the year. A smaller generator on a larger wing will more frequently run at its rated capacity, which provides a less variable power generation during the year. The same capacity development pursuing the same reasoning of more constant generation can also be seen for traditional wind turbines [56]. Lower variability gives the power-generation profile greater value and simplifies implementation in the power system. These results suggest that if a smooth annual power generation is targeted, a wing should be designed with a high area-to-weight ratio, and a reasonable rated capacity. Furthermore, the lighter the wing, the higher the power yield. However, all of these design choices come with a higher economic investment cost.

Second, the local wind conditions are also a decisive factor for the AWES performance. The results show that high wind shear, i.e. a large difference between high-altitude and low-altitude wind speeds, results in a lower correlation between the generation profile of an AWES and the generation profile of a WT. Thus, there are more times at which one technology generates electricity, while the other one cannot supply due to a lack of wind at its operational altitude. As a result, at locations with a high wind shear, the two technologies are more likely to complement each other and provide a smoother wind power generation when combined.

This study only considers drag-mode systems. Pumping-mode systems differ significantly in how they transform wind energy into electrical energy. However, the same wind resource is harvested and the overall performances at an hourly time scale are likely to be similar. Hence, the finding of the two decisive factors, wing design and wind shear, can be assumed valid in the case of the pumping-mode system, too.

So far, the differences in the power-generation profiles of the individual wind power systems have been investigated, providing a good direct comparison between AWESs and WTs. In order to investigate the actual economic value of generation profiles provided by AWESs, the technology is implemented in the regional electricity-system model, presented in Section 4.2.2.

Value of AWE in the electricity generation system
The results of implementing AWES farms into the electricity-system model show that

- the resulting Marginal System Value (MSV) of AWESs varies by region and wing size, resulting in a range between 1.3 and 2.2$^{M€}$/MW at low AWE shares and between 0.4 and 1$^{M€}$/MW for high AWE shares. Here, "AWE share" refers to the share of total electricity that is produced by AWESs. This value can be seen as an upper bound of the present value of capital and O&M costs in a 30-year life time that would be financially viable in a power system. As a comparison, the corresponding WT costs are estimated at 1.5$^{M€}$/MW for the year 2050. The LCOE[9] can be estimated by multiplying the MSV with the annuity factor and dividing by the annual FLHs of the actual producing systems. This yields a range of 35-45 $^{M€}$/MWh, which denotes the maximal LCOE allowed in order to be cost-competitive in the future electricity system. This level can be compared to the estimated range of 33$^{€}$/MWh and 150$^{€}$/MWh, stated in the work of [3, 4, 15, 16].

- the MSV differs greatly between the large and small wing, which is due to the level of variability of the annual power-generation profile and the FLHs. For an illustration, the FLHs of the three wind-power systems are visible for the cases of Sweden and Spain (see Fig. 4.2).

- the total wind energy share (AWESs and WTs) in the electricity system is not increased by introducing AWESs. This is due to their very similar generation profiles, which lead to simply replacing the other technology dependent on their respective system cost.

- in regions with generally good wind conditions, the value of AWE is highest when replacing traditional WTs at poor wind sites, while leaving the high-wind sites to the traditional WTs. This way of allocating AWESs and traditional WTs within a region uses the advantages of each technology: the partly higher FLHs of AWESs relative to WTs and the less variable electricity generation of WTs.

We find that our results on the economic value of AWESs are determined by the following three factors: the share of AWE in the electricity system, the AWE power density, and the profile value.
First, the results are determined by the share of AWE in the electricity system. The MSV of AWE clearly drops as the share of AWE in the total

---

[9]Levelized cost of energy

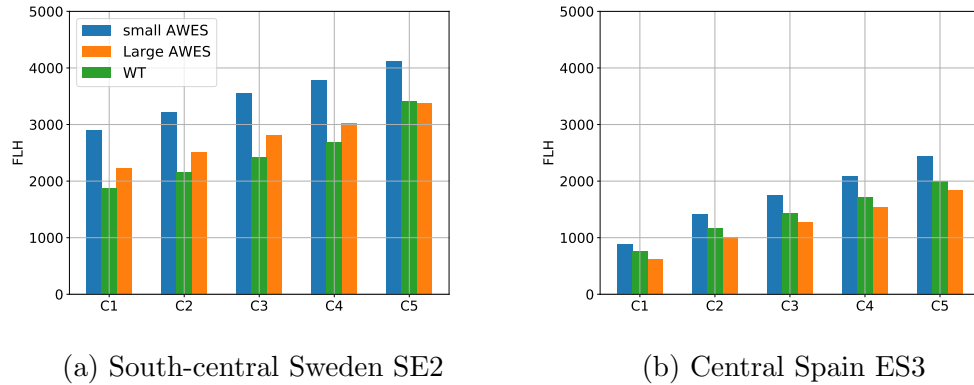(a) South-central Sweden SE2   (b) Central Spain ES3

Figure 4.2: Full Load Hours (FLH) for all five wind classes for all modelled wind power technologies, the small AWES, the large AWES, and the WT are shown for the windy region of south-central Sweden (left) and the less windy region of central Spain (right). Overall, the small AWE system shows the highest FLHs.

electricity supply increases. This is caused by an increased need for thermal generation to balance variable electricity generation and by the eventual system saturation of power produced by the wind power technologies.

Second, the results are determined by the power density (GW per km^2 ground area) of the AWESs. The greater the density, the greater the value of the technology. The density is determined by the farm density as well as the area availability, which is influenced by social acceptance and regulations. Increasing the farm density or the area availability allows for allocating more capacity at high wind-speed sites, which improves the value of the system as more power can be produced per installed capacity.

Third, the results are determined by the number of FLHs for the AWESs as well as the temporal distribution of the power generation (i.e. profile value). Comparing the two modelled AWESs, the small wing has a lower weight-to-area ratio ($29 < 42$ $^{kg}/_{m^2}$) and a lower specific power[10] ($18.6 < 28.5$ $^{kW}/_{m^2}$). Both wing design aspects have a major impact on the power-generation performance.

The results are affected by assumptions and simplifications made in the modelling. In order to study the pure regional dynamics, regions are modelled in isolation, which means that electricity trading is not taken into account. Further, storage devices and demand-side management are not included in the modelling. This limits the regional and temporal smoothing

---

[10]Power capacity per wing area

of the power generation. Another simplification is made when implementing the wind power technologies. Even though a generation profile is available at a fine spatial resolution, these profiles are aggregated in five wind classes, with five representative profiles for each region. The representative profiles are the averaged profiles that fall within a certain wind class. This simplification smooths the regional power generation, and it assumes a geographically smooth distribution of investments across each wind class and without any grid bottlenecks. The simplifications mentioned in previous sections, like the parameter choices in the AWES model and the limitation of evaluating the drag-mode system only, are also simplifications in this study.

Conclusions

The analyses of the electricity generation of AWESs can be summarized as a handful of factors that are required for successful large-scale deployment of AWESs.

- For an AWE wind farm, a smooth power output can be realized via a reasonable control strategy that ensures synchronous flight operation of the individual systems. The power performance losses due to the restricted individual optimal operation are found to be below 4%.

- The wing design should be optimized for the desired performance. A high area-to-weight ratio is advantageous for improving the power yield per unit of installed capacity. Additionally, the lower the rated capacity of the wing compared to its area, the more often the rated capacity is reached during operation. As a result, power generation is less variable over a longer time period. This could be advantageous for the economic value of the AWE generation profile. However, this presents a trade-off as a lower rated capacity implies a lower maximal power, and a higher economic investment.

- It is unlikely that integration of AWESs into the power system increases the total share of wind energy in the electricity mix, as the generation profiles of AWESs and WTs are quite similar. Hence, instead of coexisting, the technologies replace each other depending on their respective electricity-generation costs.

- An economically advantageous coexistence of WTs and AWESs is most likely at locations with high wind shear. The greater the difference between high- and low-altitude winds, the greater is the difference in the power-generation profiles for the two technologies. A difference in profiles means that the technologies complement each other and the total electricity generation is less variable. The more

63

they complement each other, the lesser the need for other balancing technologies and the greater the possible total share of wind energy in the system.

- AWESs are most financially viable in the power system when replacing traditional wind turbine installments at sites with relatively poor wind resources at 100 m altitude. An optimal allocation of WTs and AWESs within a certain region shows that WTs should be installed at the high wind-speed sites, while AWESs are established at less windy sites. This is the most economically advantageous for three reasons. First, AWESs can harvest winds at higher altitudes, which is advantageous at sites where the wind resource is low at 100 m. Second, the numbers of FLHs for AWESs are partly higher compared to WTs throughout the wind classes. Third, WTs show a less variable annual generation, which should be exploited on the sites with a rich wind resource.

- Given the modelled cases, the cost-competitiveness of AWESs depends on wing design, location, farm density, and its actual share of the electricity supply. The AWES marginal system value ranges between 0.4 and 2.2 M€/MW, which equals 26% to 140% of the cost of traditional wind turbines. This result corresponds to a maximum "allowed" LCOE for AWESs of approximately 35-45 M€/MWh in order to be cost-competitive in the future electricity system, which is within the expected lower bound stated in [3, 4, 15, 16].

5

Summary of included papers

This chapter provides a short summary of the published papers included in this thesis.

Paper A

E.C. Malz, J. Koenemann, S. Sieberling, and S. Gros, "A reference model for airborne wind energy systems for optimization and control", *Renewable Energy*, Vol 140, pp.1004-1011, 2019.

The contribution of this paper is a point-mass model of a pumping-mode AWES based on rigid wings. The model describes the flight dynamics of a tethered six-degrees-of-freedom (DOF) rigid-body aircraft in the form of differential-algebraic equations, based on Lagrangian dynamics. With the help of a least-squares fitting approach, the model is validated using real flight data from the Ampyx Power prototype AP2. The model equations are smooth and have low symbolic complexity, so as to make the model ideal for optimization and control. The entire model formulation, including the aerodynamic model parameters are given in the paper, which aims to provide the AWE research community a model that has been validated against measured flight data and that is well suited for trajectory and power output simulation and optimization.

Paper B

E.C. Malz, V. Verendel, S. Gros, "Computing the power profiles for an airborne wind energy system based on large-scale wind data", in press in *Renewable Energy, 2020*.

This work develops a methodology to obtain the power-generation profile of an AWES by implementing real wind data into a power-maximizing optimal control problem that is discretized into an NLP and solved with the primal-dual interior point (PDIP) solver IPOPT. Computing the annual generation profile at different locations requires a large family of NLPs to be solved sequentially for the individual wind parameters. As the NLP is highly nonlinear and complex to solve, a homotopy-path-following strategy is proposed to reduce the computation time. An algorithm is presented that, with the help of small modifications to the PDIP solver, efficiently solves the NLP for the large number of wind parameters. For very extensive wind data the use of a regression model is proposed, learning the mapping of wind parameters and optimal power production. The application of the algorithm reduces the computation time for the generation profile significantly.

Paper C

E.C. Malz, M. Zanon, S. Gros, "A Quantification of the Performance Loss of Power Averaging in Airborne Wind Energy Farms", *European Control Conference (ECC)*, 2018.

This work uses the model developed in Paper A to investigate power fluctuations of a temporal sub-minute scale in a potential AWE farm. Drag-mode and especially pumping-mode systems have large periodic power-generation fluctuations, which might become a significant obstacle to large-scale deployment of AWESs in the power grid. In an AWE farm, these periodic power fluctuations can be mitigated by synchronizing and phase-shifting the individual flight trajectories, so that the total farm power is averaged. However, this trajectory control removes the possibility for individual AWE systems within a wind farm to optimize their orbit time for their specific, local wind conditions, entailing a loss of performance. The loss of performance is quantified in this paper for different wind speeds and distributions across the farm.

Paper D

E.C. Malz, F. Hedenus, L.Göransson, V. Verendel, S. Gros, "Drag-mode airborne wind energy vs. wind turbines: An analysis of power production, variability and geography", *Energy*, Vol 193, 2020.

This work focuses on comparing the generation profiles of drag-mode AWESs and traditional wind turbines. The annual generation profiles of different AWESs are computed for different regions with the help of the algorithm developed in Paper B. These results are then analysed using three performance indicators: the total annual power generation (load duration curve), the Gini coefficient, and the correlation coefficient. The results show that AWESs with smaller wings have the highest annual production per unit of installed capacity among the modelled systems. The AWE power generation of all AWESs correlates in time at all sites with the production of WTs, and the Gini coefficients are similar. This observation indicates that AWESs and WTs provide a similar generation profile, and thus AWESs need to show a lower cost than the well-established WTs in order to be competitive. The results show that the wing design as well as the local wind shear are crucial factors that determine the actual AWE performance.

Paper E

E.C. Malz, L.Göransson, S. Gros, "The Value of Airborne Wind Energy to the Electricity System", submitted to *Wind Energy, Wiley.*

This work investigates the value of AWESs in a future electricity generation system. Fine spatio-temporal wind data are used to estimate the annual power-generation profiles per grid point within the model regions of Ireland, Hungary, central Spain, and south-central Sweden. The generation profiles are implemented in an electricity-system model and the total system costs are minimized. The value of AWESs in the system is investigated by fixing a certain electricity share to be supplied by AWESs. The main factors that influence the value of AWESs are found to be the Full Load Hour (FLH), the profile value, and the power density of the system. Results show that due to similar generation profiles, AWESs and WTs are not complementary technologies, but rather replace each other dependent on their relative costs. In order to be cost-competitive at low AWE shares of the total mix, the maximal marginal system values vary between 1.3 and 2.2 €/MW dependent on case and location.

6

Discussion, conclusions and future work

This chapter relates the work performed in this thesis to the original research motivations formulated in Section 1.2 by discussing and reflecting on the work (Section 6.1), concluding the work (Section 6.2), and offering an outlook on future work (Section 6.3).

6.1 Discussion

"Airborne Wind Energy - To fly or not to fly?" - The question of whether and in which circumstances AWE systems will be part of the future electricity system motivates the studies of AWE power production presented in this thesis.

The results and conclusions obtained from the work are highly dependent on model choices, wind data, and assumptions and limitations made during the studies. The most influential factors are discussed in this section.

In this work, the power generation of an AWES is computed using an optimal control approach, but there are indeed other methods to chose from. By choosing optimal control, the AWES is modelled with an optimistic approach. The power production of a flight orbit is always optimized to the given external conditions, such that the modelled system yields its maximal possible power production at any instance. In practice, these power generation maxima are seldom reached, as disturbances, and measurement and estimation errors, tend to degrade the operation performance of the system. Additionally, launching, landing, and aligning with the current wind direction reduces the power output further, which is not taken into account in this work. The conclusions on the power potential of the modelled AWESs

are thus based on optimistic modelling results. So, even if the model used in this thesis for obtaining large-scale power generation data is considered simplistic, more detailed and sophisticated methods of power estimation would probably lead to similar or lower power generation estimations.

The design of the modelled AWESs has a great impact on the computed absolute value of the power generation, which has to be considered when evaluating the results. The conclusions drawn from the studies take this design aspect into account. Further, the density of the individual systems within a wind farm is a decisive factor in terms of competition with other renewable energy technologies. In this thesis, a conservative spacing determined by the tether length has been chosen. With sufficient AWES control, farm spacing could be reduced, however it is yet unknown what can be realized in the future. In decisions on geographical sites or system design, these influential aspects are important to take into account.

The power production has been computed for many different locations and regions using MERRA-2 (Paper D) and ERA5 wind data (Paper E). These data sets are obtained by reanalyses and hence are only modelled approximations of the actual wind speeds. MERRA-2 data have a relatively low spatial resolution of $0.625° \times 0.5°$, which in Sweden corresponds to an area of approximately $38 \times 57 \, \text{km}^2$. Additionally, in complex terrain MERRA-2 shows a relatively weak correlation (0.75) and a high bias (1.35m/s) in wind speed estimation to measurement data [57] at 50-100 m above ground. ERA5 wind data show a higher resolution of $0.25° \times 0.25°$, which in Sweden corresponds to an area of approximately $15 \times 28 \, \text{km}^2$. Compared to MERRA-2, ERA5 shows a stronger correlation and lower bias to measured wind data at the low altitudes, but still underestimates wind speeds [57]. Hence, the absolute values of the computed power production for the wind turbine might be incorrect for some sites and regions. As the wind data used for the AWESs is from higher altitudes, the error in absolute values of wind speeds is unknown and could be different. However, the conclusions in Papers D and E are nevertheless indicative even if the absolute production values should not be taken literally.

In order to evaluate the economic value of the AWE technology, the generation profiles of different system designs are implemented in an investment and dispatch model of an electricity generation system modelled with net-zero CO_2 emissions. The purpose of the model is to study the dynamics of an eventual future electricity system. The model is built as a green-field model, i.e. no previous investments in technologies are taken into account. Transmission losses or grid bottlenecks within a modelled region are not taken into account, dismissing local differences that are given by grid constraints. Storage and demand-side management technologies are not modelled, which

removes the option of shifting power loads in time. Further simplification is made as inter-regional trading is not modelled, which removes the possibility of exporting or importing electricity for balancing generation and load. In fact, including these devices in the system would smooth the variability of wind power and reduce the impact of the profile values and potentially also increase the total share of wind power in the system. On the other hand, the power-generation profiles of both WTs and AWESs are already smoothed, as they are averaged and aggregated into five different wind profiles over the region. This might remove detailed profile information but is comparable to the smoothing of the total wind power generation over a large region. The electrification of the transport, industry, and heating sectors is an important aspect when modelling the future electricity system. This thesis only models the electricity sector, while the mentioned sectors are not considered. Hence, it is unclear if and how the inclusion of these sectors would affect the integration of AWESs in the electricity system and their interaction with WTs.

There are other relevant topics, important to the assessment of the AWE potential but not analysed further in this thesis. First, there are sites that are possibly easier to exploit by AWESs than by traditional wind turbines. For example, deep offshore locations are only an option when using floating platforms, which are easier to realize for AWESs. Second, this thesis investigates the power potential for drag-mode systems only. There are other crosswind system designs available, such as the pumping-mode system or multiple-kite systems, that might lead to different conclusions. The latter is an interesting case, as a static main tether reduces the tether drag for the individual AWESs, allowing for higher altitudes to be reached [6, 58, 59].

6.2 Conclusions

Airborne wind energy is a new wind power technology meant to overcome limitations pertaining to altitude and materials that affect traditional wind turbines. The proclaimed expected advantages of the tethered power-producing wing are greater power yield and reduced usage of materials and thus lower costs for generating power.

Many of these qualities remain to be proven in reality. A report of the EU commission [15] lists barriers and recommendations for the commercialization of the AWE technology. The barriers named are e.g. airspace restrictions, social acceptance, and competition with well-established renewable energy systems. This entails that if a new power production technology aims for large-scale commercialization, either the costs have to be low or the amount and value of the power and electricity generation need to be

71

high. The latter aspect is investigated in this work.

This thesis analyses the power production at the sub-minute scale as well as the electricity generation over a longer time frame for some AWES designs. The tools used for the analyses are presented in detail in order to allow further research on the power generation of AWESs. A reference model of an AWES is formulated and implemented in an optimal control framework in order to compute the maximum average power generation during one flight orbit. This OCP is then used to answer research questions regarding wind farm control, annual generation profiles, and the value of AWESs in the power system. Real wind data are implemented, such that the power can be computed for specific time intervals and locations. In order to compute annual power-generation profiles, the thesis provides a strategy for solving large numbers of OCPs, maximizing the power generation of the AWES in a computationally efficient way.

Based on this work, the following conclusions can be drawn:

- The developed AWES model describes the flight dynamics including the motions of the wing as well as tether and aerodynamic forces. The model is formulated assuming a straight tether using differential algebraic equations. In this thesis, the model is validated with real flight data, obtained from the company Ampyx Power that develops a pumping-mode AWES. The validation is performed by fitting the model trajectory to the measurement data, including flight trajectory positions, wing motions, control inputs, and tether force. The results show that the power production computed via the model is a valid estimation of the actual production, presenting a relative error of 0.92% between model simulation and data measurements.

- An OCP is formulated, implementing the AWES model to optimize the average power generation with respect to external parameters. The aspect of wind farm control has been analysed by quantifying the power loss when synchronizing the flight trajectories of AWESs within a farm. An individual power optimization per system subjected to local wind speeds would result in the total maximal power generation of the wind farm but also bears the risk of superimposing fluctuations. Instead, the trajectories may be optimized subjected to the average wind speed of the farm, such that all flight trajectories are the same and can be phase shifted. We find that with the modelled system types, a maximum of 4% of the possible maximal farm power is lost.

- From the systems modelled in the thesis, it can be concluded that the annual generation profile of AWESs is quite similar to the modelled WT generation profile. This entails that an implementation of

AWESs in the electricity system in general does not increase the total electricity share provided by wind energy. Instead, the two wind power technologies simply replace each other dependent on their system costs. Note that in this work, only the electricity sector is modelled, and storage and demand side management are not taken into account. The most economically viable allocation has found to place WTs at the high wind-speed sites, while AWESs take the lower wind-speed sites (relative to wind speeds at 100 m). The generation profiles of AWESs and the WTs tend to be less similar at high wind shears, i.e. high differences between low- and high-altitude winds.

- The economic value of AWESs is dependent on the characteristics of the annual generation profile. Factors that influence the profile are found to be the wing design (area, weight, and generator capacity), which determines FLHs and the variability of the generation profile. Further, the power density in wind farms and the total available area are decisive factors that define the maximal cost allowed in order to be cost-competitive for large-scale deployment.

- The thesis analyses the marginal system value of the modelled AWESs, which relates to the economic value of the power they generate. The value is found to lie within the range of 1.3 and 2.2 M€/MW if AWE has a small share in the total electricity production and tends to decrease for greater shares. These values relate to a maximum LCOE for AWESs between approximately 34 and 44 M€/MWh in order to be cost-competitive in the future power system. These results are comparable to the lower bound of the estimated costs stated in previous work, which are given between 33 €/MWh and 150 €/MWh.

All in all, this thesis investigates multiple factors that influence the power potential of AWESs and hence the economic value of the technology. The factors may contribute to choosing the right incentives for the future development of AWE. However, whether, and to what extent, we will have flying wind power systems in the end is still an open question. The answer to "To fly or not to fly?" is, as so often: It depends.

6.3 Future Work

The estimated power potential of AWESs is crucial for planning the future development of the technology. Thus, as future work the potential power generation of the pumping-mode and dual-kite systems may be investigated. Further, the integration of AWESs into the future electricity system needs to

be analysed further and in more detail. More or different technologies may be included in the electricity-system model, other sectors need to be taken into account, and the impacts of inter-regional trade and intra-regional grid congestion need to be investigated.

References

[1] Ampyx power. https://www.ampyxpower.com, (Accessed on: June 10, 2020).

[2] Kitegen. http://www.kitegen.com/en/, (Accessed on: June 10, 2020).

[3] Kitepower. Kitepower - airborne wind energy. https://kitepower.nl, (Accessed on: June 10, 2020).

[4] Enerkite. https://www.enerkite.de, (Accessed on: June 10, 2020).

[5] Twintec. http://twingtec.ch, (Accessed on: June 10,2020).

[6] Kiteswarms. https://kiteswarms.com, (Accessed on: June 10, 2020).

[7] S. Watson et al., "Future emerging technologies in the wind power sector: A european perspective," *Renewable and Sustainable Energy Reviews*, vol. 113, p. 109270, 2019.

[8] A. Cherubini, A. Papini, R. Vertechy, and M. Fontana, "Airborne wind energy systems: A review of the technologies," *Renewable and Sustainable Energy Reviews*, vol. 51, pp. 1461 – 1476, 2015.

[9] M. Diehl, "Airborne wind energy: Basic concepts and physical foundations," in *Airborne Wind Energy*, U. Ahrens, M. Diehl, and R. Schmehl, Eds.   Springer, 2013, pp. 3–22.

[10] M. L. Loyd, "Crosswind kite power," *Journal of Energy*, vol. 4, pp. 106–111, Jun. 1980.

[11] Makani power. https://makanipower.com, (Accessed on: June 10, 2020).

[12] Siemens Gamesa. https://www.siemensgamesa.com/, (Accessed on: June 10, 2020).

REFERENCES

[13] Eric Lantz et al, "Increasing wind turbine tower heights: Opportunities and challenges," National Renewable Energy Laboratory (NREL), Tech. Rep., 2019. [Online]. Available: https://www.nrel.gov/docs/fy19osti/73629.pdf

[14] MHI Vestas. Innovations - Offshore Wind Turbines. https://mhivestasoffshore.com/, (Accessed on: June 10, 2020).

[15] European Commission, "Study on challenges in the commercialisation of airborne wind energy systems," Publications Office of the European Union, Available at: https://op.europa.eu/en/publication-detail/-/publication/a874f843-c137-11e8-9893-01aa75ed71a1, (Accessed on: June 10, 2020), Tech. Rep., September 2018.

[16] S. Mann, "An introduction to airborne wind technology and cost reduction trends," *An Introduction to Airborne Wind Technology and Cost Reduction Trends*, February 2019. [Online]. Available: https://ore.catapult.org.uk/analysisinsight/an-introduction-to-airborne-wind

[17] L. Fagiano, M. Milanese, and D. D. Piga, "Optimization of airborne wind energy generators," *International Journal of Robust and Nonlinear Control*, vol. 22, no. 18, pp. 2055–2083, 2012.

[18] C. L. Archer, L. Delle Monache, and D. Rife, "Airborne wind energy: Optimal locations and variability," *Renewable Energy*, vol. 64, pp. 180–186, 2014.

[19] M. Sommerfeld, C. Crawford, A. Monahan, and I. Bastigkeit, "Lidar-based characterization of mid-altitude wind conditions for airborne wind energy systems," *Wind Energy*, vol. 22, no. 8, pp. 1101–1120, 2019.

[20] P. Bechtle, M. Schelbergen, R. Schmehl, U. Zillermann, and S. Watson, "Airborne wind energy resource analysis," *Renewable Energy*, vol. 141, pp. 1103–1116, 2019.

[21] M. Diehl, "Numerical optimal control," (Accessed on: June 10, 2020), Available at: https://www.fs.isy.liu.se/Edu/Courses/NumericalOptimalControl/Diehl_NumOptiCon.pdf.

[22] M. Zanon, "Efficient nonlinear model predictive control formulations for economic objectives with aerospace and automotive applications," Ph.D. dissertation, KU Leuven, Faculty of Engineering Science, 2015.

76

[23] L. Biegler, *Nonlinear Programming.* Society for Industrial and Applied Mathematics, 2010.

[24] A. Wächter and L. T. Biegler, "On the implementation of an interior-point filter line-search algorithm for large-scale nonlinear programming," *Mathematical Programming*, vol. 106, no. 1, pp. 25–57, 2006.

[25] J. Lundgren, M. Rönnqvist, and P.Värbrand, *Optimization.* Studentlitteratur AB, 2010.

[26] D. S. Naidu, *Optimal control systems*, R. C. Dorf, Ed. CRC Press, 2003.

[27] S. Gros and M. Diehl, "Modeling of airborne wind energy systems in natural coordinates," in *Airborne Wind Energy*, U. Ahrens, M. Diehl, and R. Schmehl, Eds. Berlin, Heidelberg: Springer, 2013, pp. 181–203.

[28] J. Koenemann, P. Williams, S. Sieberling, and M. Diehl, "Modeling of an airborne wind energy system with a flexible tether model for the optimization of landing trajectories," *IFAC-PapersOnLine*, vol. 50, pp. 11 944 – 11 950, 2017.

[29] G. Horn, S. Gros, and M. Diehl, *Numerical Trajectory Optimization for Airborne Wind Energy Systems Described by High Fidelity Aircraft Models.* Berlin, Heidelberg: Springer, 2013, pp. 205–218.

[30] G. Licitra, J. Koenemann, A. Bürger, P. Williams, R. Ruiterkamp, and M. Diehl, "Performance assessment of a rigid wing airborne wind energy pumping system," *Energy*, vol. 173, pp. 569 – 585, 2019.

[31] G. Licitra, J. Koenemann, P. Williams, G. Ruiterkamp, R.and Horn, and M. Diehl, "Viability assessment of a rigid wing airborne wind energy pumping system." in *Proceedings of the 2017 21st International Conference on Process Control, PC 2017*, 2017, pp. 452–458.

[32] M. Ranneberg, D. Wölfle, A. Bormann, P. Rohde, F. Breipohl, and I. Bastigkeit, "Fast power curve and yield estimation of pumping airborne wind energy systems," in *Airborne Wind Energy: Advances in Technology Development and Research*, R. Schmehl, Ed. Springer, 2018, pp. 623–641.

[33] J. P. R. Machado, *Estimation of energy production in aerial systems of Wind Energy*, Msc Thesis, University of Porto, 2019.

REFERENCES

[34] S. Costello, G. François, and D. Bonvin, "Crosswind kite control – a benchmark problem for advanced control and dynamic optimization," *European Journal of Control*, vol. 35, pp. 1 – 10, 2017.

[35] L. Landberg, *Meteorology for wind energy: an introduction*, 1st ed. Wiley, 2016.

[36] R. Gelaro et al., "The modern-era retrospective analysis for research and applications, version 2 (merra-2)," *Journal of Climate*, vol. 30, no. 14, pp. 5419–5454, 2017.

[37] Copernicus climate change service (c3s) : Era5: Fifth generation of ecmwf atmospheric reanalyses of the global climate. Available at: https://www.ecmwf.int/en/forecasts/datasets/reanalysis-datasets/era5, (Accessed on: June 10, 2020).

[38] I. Argatov and S. Risto, *Efficiency of Traction Power Conversion Based on Crosswind Motion.* Springer Berlin Heidelberg, 2013, pp. 205–218.

[39] J. D. Anderson, *Fundamentals of Aerodynamics*, 6th ed. Mc Graw Hill Education, 2017.

[40] C. Harham, "Response to the federal aviation authority," Makani Power, Available at http://www.energykitesystems.net/FAA/FAAfromMakani.pdf, Tech. Rep., 2012.

[41] J. Kolar, T. Friedli, F.Krismer, A. Looser, and M. Schweizer, "Conceptualization and multi-objective optimization of the electric system of an airborne wind turbine," *2011 IEEE International Symposium on Industrial Electronics*, pp. 32–55, 2011.

[42] D. V. Lind, "Analysis and flight test validation of high performance airborne wind turbines," in *Airborne Wind Energy*, U. Ahrens, M. Diehl, and R. Schmehl, Eds. Springer, 2011, pp. 473–490.

[43] F. Bauer et al., "Drag power kite with very high lift coefficient," *Renewable Energy*, vol. 118, pp. 290–305, 2018.

[44] S. Gros and M. Zanon, "Numerical optimal control with periodicity constraints in the presence of invariants," in *IEEE Transactions on Automatic Control*, vol. 63, 09 2019, pp. 2818–2832.

[45] S. Gros, M. Zanon, and M. Diehl, "A relaxation strategy for the optimization of airborne wind energy systems," in *2013 European Control Conference (ECC)*, July 2013, pp. 1011–1016.

[46] Earth Data Nasa. Dataset: $merra - 2tavg1\_2d\_slv\_nx : 2d, 1 - hourly$. Available at: https://disc.gsfc.nasa.gov/datasets/M2T1NXSLV_5.12.4/summary, (Accessed on June 10, 2020).

[47] ——. Dataset: $merra - 2tavg3\_3d\_asm\_nv$. Available at: https://disc.gsfc.nasa.gov/datasets/M2T3NVASM_5.12.4/summary, (Accessed on June 10, 2020).

[48] P. Deuflhard, *Newton Methods for Nonlinear Problems*. Springer, 2004.

[49] M. Galluci, *Alphabet's Wind Energy Kites to Fly Offshore*, Available at https://spectrum.ieee.org/energywise/energy/renewables/alphabets-moonshot-wind-kites-to-fly-offshore, February 2019.

[50] T. Haas, J. De Schutter, M. Diehl, and J. Meyers, "Wake characteristics of pumping mode airborne wind energy systems," *Journal of Physics: Conference Series, Wake Conference*, vol. 1256, May 2019.

[51] U. Zillermann and P. Bechtle, "Emergence and economic dimension of airborne wind energy," in *Airborne Wind Energy: Advances in Technology Development and Research*, R. Schmehl, Ed. Springer, 2018, pp. 1–25.

[52] Wind Europe, *Wind energy in Europe: Scenarios for 2030*, September 2017, accessible at https://windeurope.org/wp-content/uploads/files/about-wind/reports/Wind-energy-in-Europe-Scenarios-for-2030.pdf.

[53] H. Holttinen, S. Rissanen, X. Larsen, and A. L. Løvholm, "Wind and load variability in the nordic countries," *VTT Technical Research Centre of Finland*, 2013, Available at: http://www.vtt.fi/publications/index.jsp (Accessed on: August 05, 2020).

[54] *Vestas 2 MW platform*. [Online]. Available: http://nozebra.ipapercms.dk/Vestas/Communication/Productbrochure/2MWbrochure/2MWProductBrochure/?page=1

[55] R. Dorfman, "A formula for the gini coefficient," *The review of economics and statistics*, vol. 61, pp. 146–159, 1979.

[56] IRENA, *Renewable Power Generation Costs in 2018*, International Renewable Energy Agency, Abu Dhabi, 2019.

[57] B. Jourdier, "Evaluation of era5, merra-2, cosmo-rea6, newa and arome to simulate wind power production over france," *Advances in Science and Research*, vol. 17, pp. 63–77, 2020. [Online]. Available: https://asr.copernicus.org/articles/17/63/2020/

[58] R. Leuthold, D. S. Jochem, E. C. Malz, G. Licitra, S. Gros, and M. Diehl, "Operational regions of a multi-kite awe system," in *2018 European Control Conference (ECC)*. IEEE, 2018, pp. 52–57.

[59] M. Zanon, S. Gros, J. Andersson, and M. Diehl, "Airborne wind energy based on dual airfoils," *IEEE Transactions on Control system technology*, vol. 21, pp. 1215 – 1222, 2013.